BOSTON UNIVERSITY

GRADUATE SCHOOL OF ARTS AND SCIENCES

Dissertation

PHYSICS OF FLOW IN RANDOM MEDIA

by

EDUARDO LOPEZ

B.S., Universidad del Zulia, 1995
M.A. Boston University, 2001

Submitted in partial fulfillment of the

requirements for the degree of

Doctor of Philosophy

2005

Approved by

First Reader ____

H. Eugene Stanley, Ph.D.
University Professor, Professor of Physics,
Director of Center for Polymer Studies

Second Reader ____

William Skocpol, Ph.D.
Professor of Physics

DEDICATION

To Eduardo R. López

May your spirit always be in our lives.

ACKNOWLEDGMENTS

I am thankful to the many people that have offered their help to me along the long path to achieving this goal.

Sergey Buldyrev, Shlomo Havlin and Lidia Braunstein for serving as mentors and friends through the years of learning and growing.

To Mirtha Cabello, Adriana Estrella and Evelio Estrella who in their own ways helped me the difficult years this program required.

To Gene Stanley, for opening the door to opportunities that would had been out of reach otherwise.

To my good friends in Boston.

To my all the teachers that have been there along the way.

To my lovely Kaleena.

And lastly, to my loving family, which gave me endless support and love to prepare me for whatever challenge life would give me.

Eduardo
March 2005

PHYSICS OF FLOW IN RANDOM MEDIA

(Order No.)

EDUARDO LOPEZ

Boston University Graduate School of Arts and Sciences, 2005

Major Professor: H. Eugene Stanley, Professor of Physics.

ABSTRACT

An important problem is the construction of theories relating geometry of random structures with flow properties in those structures, because the results have implications in oil recovery, metabolic network research and polymer physics. For this reason, I consider three kinds of random structures and elucidate their flow properties.

Firstly, to improve oil production forecasting, I study traveling-tracer times $t_{\rm tr}$ between sites A and B (injection and extraction) separated by distance r in percolation systems of linear size L through their probability density function (pdf) $P(t_{\rm tr}|r, L)$. I find: (a) a most probable traveling time $t^*_{\rm tr}$ satisfying a power law with r, and (b) two power law decay regions for $P(t_{\rm tr}|r, L)$, one for intermediate $t_{\rm tr}$ and another for large $t_{\rm tr}$ with multifractal properties. I explain these results through geometric exponents of percolation.

Secondly, I examine the pdf $P(\ell_{\rm opt}|r, L)$ of optimal path lengths $\ell_{\rm opt}$ between A and B when lattice sites are assigned weights of an exponentially broad distribution. This problem relates to polymer behavior in random potentials. I find a power law decay for $P(\ell_{\rm opt}|r, L)$, and determine the scaling form of $P(\ell_{\rm opt}|r, L)$. Since optimal paths can jump across so called 'percolation regions', $P(\ell_{\rm opt}|r, L)$ differs from $P(\ell_{\rm tr}|r, L)$, the pdf of traveling-tracer lengths $\ell_{\rm tr}$ of the first model. However, by constraining optimal paths to remain inside such percolation regions, the two problems exhibit similar scaling.

Thirdly, I analyze pdf $\Phi_{\rm SF}(G)$ of conductance G between two arbitrary nodes of random scale-free networks with degree distribution $P(k) \sim k^{-\lambda}$ or Erdős-Rényi

networks, where in both networks the links have unit resistance. I predict a power-law distribution $\Phi_{\rm SF}(G) \sim G^{1-2\lambda}$ and confirm my predictions by simulations. The power-law tail in $\Phi_{\rm SF}(G)$ leads to large values of G, improving transport in scale-free networks compared to Erdős-Rényi networks. Based on a simple physical picture that I call the transport backbone picture, I show that the conductances are $ck_Ak_B/(k_A + k_B)$ for any pair of nodes A and B with degrees k_A and k_B. Thus, a single parameter c characterizes transport on complex networks.

In summary, this work presents new ideas that illustrate the connection between flow and geometry in random structures.

Contents

List of Tables

List of Figures

Part I

Introduction

Chapter 1

Introduction. Models of Random Structures

Transport in many random structures is anomalous, i.e., different than that in regular space. Random structures are found in many places in the real world, from oil reservoirs to the Internet, making the study of anomalous transport properties a wide reaching field.

In this work, we focus on two important examples: the properties of tracers inside percolation systems, and the conductance of complex networks. These constitute examples of the most active areas of research at present. We begin in this introduction by addressing the accepted models for the above mentioned problems, and proceed to study their transport behavior through different methods in the rest of this Thesis.

Let us begin by considering the nature of an oil field, one of the most important examples of random structures due to the relevance of oil as a source of energy today. Most oil reservoirs are complicated geological structures [1] composed of several kinds of rock that have been deposited over a long period of time. The configuration of the structure has usually been altered by tectonic activity and mineral deposition by aquifer flow. For our purposes, the types of rock comprising any oil reservoir can be separated into two categories: high-permeability (conducting) and low-permeability (insulating). The location of both the conducting and insulating rock is random but also nontrivial, i.e., during extraction it is only through the conducting rock that the flow of oil occurs.

Based on the random spatial location of the conducting rock, a simplifying procedure that has emerged in attempting to predict oil extraction is to model the reservoir by a bond percolation cluster with occupation probability p [2, 3, 4, 5, 6, 7, 8, 9, 10, 11, 12, 13, 14, 15, 16, 17, 18, 19, 20]. The value of p corresponds to the fraction of conducting rock to total rock of the reservoir. This captures the essential features of the reservoir, while avoiding some of the non-crucial complications. An advantage to using percolation theory is that it makes available the already well developed percolation theory to the analysis of oil recovery. However, we must caution the reader that these approximations cannot be taken as the definitive description for oil reservoirs. It is well known [21, 22, 23, 24, 25] that true field-size porous media possess correlations. Our description merely represents a first order approximation, which can serve as a base for more detailed studies.

Percolation is a model introduced by Broadbent and Hammersley [26] to address the question of wetting inside porous rocks. Since then, it has been used for numerous applications ranging from forest fires to drug delivery [27, 2, 28]. For concreteness, we elaborate on the two-dimensional example. For a simple square of bonds (sites) of size $L \times L$, each bond is kept with the occupation probability p, or eliminated with probability $1 - p$. For small values of p below a certain critical $p = p_c$, the lattice is populated by small, disconnected clusters of bonds which are interconnected in the sense that their first neighbors are also part of the cluster. For values of $p > p_c$, a fraction of bonds of the lattice is connected in such a way that it spans the system, that is, the largest cluster reaches opposite boundaries of the system. Another property of this largest cluster is that the number of bonds belonging to it is a function of the system size L. The critical probability p_c is that for which a spanning cluster appears for the first time. The mass M of the spanning cluster has been found to be fractal in the sense that its mass dependence with size is goverened by a non-integer exponent [29]. This is

$$M \sim L^{d_f}, \tag{1.1}$$

where d_f is called the fractal dimension of the percolation cluster.

Aside from this property, percolation clusters possess other relevant features that are related to their fractal nature. For instance, when the bonds of a cluster are considered to be resistors of value one, the percolation cluster is usually called a Random Resistor Network, and the resistance R between two oppposite boundaries scales as

$$R \sim L^{\tilde{\mu}}. \tag{1.2}$$

In Chap. 2, we consider the Random Resistor Network at p_c, and place two terminals A and B (a source and a sink), between which we establish a potential (pressure) difference. Then, a stationary flux appears in the system, and drives tracer particles from source to sink (*Particle Launching Algorithm* [30]). The tracers are random walkers for which the rules of motion are governed by the stationary flux (see Chap. 2). They explore many possible paths within the percolation cluster, giving information about their traveling times. In fact this model mimics the process of secondary oil extraction, in which two or more wells are drilled into a reservoir to extract its oil. In the simple case of two wells, one of them acts as an injector A and the other as an extractor B. Through well A, a fluid such as water or steam are injected, pushing the oil inside towards the extration well B. No mixing occurs at the flux regime and scale at which the oil companies operate, and thus, we disregard such behavior here.

The conditions under which oil extraction takes place are usually one of two: constant current or constant pressure. For the constant current case, each realization of the medium (each cluster) is subjected to a pressure difference between source and sink such that the stationary flow established inside is some predetermined constant value. When the next realization is considered, the pressure is once again adjusted to attain the desired constant flux value. When constant pressure conditions are required, the pressure drop between source and sink is always the same across realizations of the medium.

We use the Particle Launching Algorithm to explore the post-breakthrough behavoir of the oil and water mix that forms at the extraction point of an oil reservoir being exploited through secondary oil extraction. We calculate and analyze the traveling time probability density function for two values of the fraction of connecting bonds p: the homogeneous case $p = 1$ and the inhomogeneous critical threshold case $p = p_c$. We analyze both constant current and constant pressure conditions at $p = p_c$. The homogeneous $p = 1$ case serves as a comparison base for the more complicated $p = p_c$ situation. We find several regions in the probability density of the traveling times for the homogeneous case ($p = 1$) and also for the critical case ($p = p_c$) for both constant pressure and constant current conditions. For constant pressure, the first region I_P corresponds to the short times before the flow breakthrough occurs, when the probability distribution is strictly zero. The second region II_P corresponds to numerous fast flow lines reaching the extraction point, with the probability distribution reaching its maximum. The third region III_P corresponds to intermediate times and is characterized by a power law decay. The fourth region IV_P corresponds to very long traveling times, and is characterized by a different power law decaying tail. The power law characterizing region IV_P is related to the multifractal properties of flow in percolation, and an expression for its dependence on the system size L is presented. The constant current behavior is different from the constant pressure behavior, and can be related analytically to the constant pressure case. We present theoretical arguments for the values of the exponents characterizing each region and crossover times. Our results are summarized in two scaling assumptions for the traveling time probability density, one for constant pressure and one for constant current. We also present the production curve associated with the probability of traveling times, which is of interest to oil recovery.

Trace traveling lengths $\ell_{\rm tr}$ are also relevant, because they inform us what are the regions of the cluster which are explored more frequently by the flow. But more surprisingly, because of some numerical coincidences, it was proposed in [12] that the traveling lengths are related to the purely static problem of finding the optimal (least cost) path length $\ell_{\rm opt}$ between two points on a lattice where there is a random cost associated to each site (bond) of the lattice, and these costs are very broad distribution. In the limit when the cost of the whole path is equal to the cost of the highest cost site along the path, we reach what is usually called the strong disorder [31], where $\ell_{\rm opt} \sim r^{d_{\rm opt}}$. In Ref. [12], it was found that $\ell_{\rm tr} \sim r^{d_{\rm tr}}$ and $d_{\rm tr} \approx d_{\rm opt}$. It was then proposed that the two problems belong to the same universality class.

In Chap. 3 we explore this conjecture, and find that, only under certain conditions this relation is true. The optimal path in strong disorder has been related to the percolation threshold p_c because the this is the ranking of the highest cost site the path typically has to crosses to connect A and B. Thus, the cost of this site, and in the strong disorder limit, the cost of the potimal path can be mapped to p_c. This relation, though, is an approximate one. In most cases, the optimal path has an energy slightly higher than the one given by the relation with p_c, because sites A and B in most cases have to travel across high energy regions before they can travel from A to B.

We show that the optimal path length distribution is, in general, different from tracer traveling path length. However, if we constrain the optimal path to have energies equal or lower than those given by p_c, then the two distributions become equivalent in that they have the smae scaling exponents. This is very relevant, because it gives a direct connection between two problems with fundamental differences: optimal path in strong disorder is a static problem, but tracer lengths in percolation is a dynamic problem.

In the last model that we study, we consider random graphs or network (also called complex networks). These are objects formed by sites and links connecting the sites randomly. There has been an explosion of research in this area with the realization that many real world networks like social, biological, computer, etc. [32] possess a structure which had not been identified. Particularly, for a site of the network, the probability distribution that it has k links, generally called degree, is given by

$$P(k) \sim k^{-\lambda} \tag{1.3}$$

where λ characterizes the probability of the network to have highly connected sites (hubs). When λ approaches a lower limit of 2, the network has a very high probability to have a site that connects to most (or even all) other sites of the network. Also, a number of anomalous properties have been identified for these networks, like a very short minimum distance between any two of its sites. This property, called the small-world property is responsible for the famous popular phrase "six degrees of separation", which simply states that there is a very short route through intermediaries (originally thought to be six by Milgram) between two individuals that do not know each other.

The competing model of networks is the Erdős-Rényi model of random graphs [33]. In it, sites are connected with probability p and disconnected with probability $1-p$, in a very similar fashion to percolation. In this case, the degree distribution is consistent with a Poisson distribution

$$P(k) \sim \frac{z^k e^{-k}}{k!}, \tag{1.4}$$

where $z \equiv \langle k \rangle = \sum_{k=1}^{\infty} kP(k)$, the average degree of the network. Mathematicians discovered critical phenomena through this model. For instance, just as in percolation on lattices, there is a critical value $p = p_c$ for which the largest connected component of the graph has a mass that scales with the system size, but below p_c, there are only small clusters.

In our study, we compare the transport property conductance, G, of the Erdős-Rényi and scale-free graphs. This is done by calculating the probability density function $\Phi(G)$ for both kinds of networks. Our study finds a sharp constrast between the two models. The scale-free networks are able to have large conductance nodes that are absent in Erdős-Rényi networks. This is found to be a consequence of the much broader distribution of degrees compared to the Poisson distribution for the Erdős-Rényi model.

In our case, we study transport for values of $p > p_c$, which are more frequently found in real systems and thus, are more important for current applications. Additionally, transport near percolation tends to be very simple for complex networks, because the structure of the percolation cluster is tree-like [34], giving almost trivial properties to $\Phi(G)$. However, for $p > p_c$ we predict a broad range of values of G, with a power-law tail distribution $\Phi_{\rm SF}(G) \sim G^{-g_G}$, where $g_G = 2\lambda - 1$, and confirm our predictions by simulations. The power-law tail in $\Phi_{\rm SF}(G)$ leads to large values of G, thereby significantly improving the transport in scale-free networks, compared to Erdős-Rényi random graphs where the tail of the conductivity distribution decays exponentially. Based on a simple physical "transport backbone" picture we show that the conductances are well approximated by $ck_Ak_B/(k_A + k_B)$ for any pair of nodes A and B with degrees k_A and k_B. Thus, a single parameter c characterizes transport on scale-free networks.

Throughout this Thesis, the importance of the interaction between the structure of the medium and the rules of flow are highlighted. We present several results which are a consequence of this relation. Yet, the major challenge of explaning dynamical properties from structural properties remains an open field which continues to offer new and interesting problems.

Part II

Tracer Flow in Percolation

Chapter 2

Post-Breakthrough Behavior in Flow through Porous Media

2.1 Overview

We numerically simulate the traveling time of a tracer in convective flow between two points (injection and extraction) separated by a distance r in a model of porous media, $d = 2$ percolation. We calculate and analyze the traveling time probability density function for two values of the fraction of connecting bonds p: the homogeneous case $p = 1$ and the inhomogeneous critical threshold case $p = p_c$. We analyze both constant current and constant pressure conditions at $p = p_c$. The homogeneous $p = 1$ case serves as a comparison base for the more complicated $p = p_c$ situation. We find several regions in the probability density of the traveling times for the homogeneous case ($p = 1$) and also for the critical case ($p = p_c$) for both constant pressure and constant current conditions. For constant pressure, the first region I_P corresponds to the short times before the flow breakthrough occurs, when the probability distribution is strictly zero. The second region II_P corresponds to numerous fast flow lines reaching the extraction point, with the probability distribution reaching its maximum. The third region III_P corresponds to intermediate times and is characterized by a power law decay. The fourth region IV_P corresponds to very long traveling times, and is characterized by a different power law decaying tail. The power law characterizing region IV_P is related to the multifractal properties of flow in percolation, and an expression for its dependence on the system size L is presented. The constant current behavior is different from the constant pressure behavior, and can be related analytically to the constant pressure case. We present theoretical arguments for the values of the exponents characterizing each region and crossover times. Our results are summarized in two scaling assumptions for the traveling time probability density, one for constant pressure and one for constant current. We also present the production curve associated with the probability of traveling times, which is of interest to oil recovery.

2.2 Preliminaries

The problem of oil extraction from a reservoir and how this extraction evolves in time, is of significance to oil companies. In order to maximize profits, they must be able to predict how much oil is recoverable from a reservoir over a given period of time. This problem can be approached scientifically by devising a model that accurately predicts the behavior of oil during the extraction process.

Most oil reservoirs are complicated geological structures [1] composed of several kinds of rock that have been deposited over a long period of time. The configuration of the structure has usually been altered by tectonic activity and mineral deposition by aquifer flow. For our purposes, the types of rock comprising any oil reservoir can be separated into two categories: high-permeability (conducting) and low-permeability (insulating). The location of both the conducting and insulating rock is random but also nontrivial, i.e., during extraction it is only through the conducting rock that the flow of oil occurs.

Based on the random spatial location of the conducting rock, a simplifying procedure that has emerged in attempting to predict oil extraction is to model the reservoir by a bond percolation cluster with occupation probability p [2, 3, 4, 5, 6, 7, 8, 9, 10, 11, 12, 13, 14, 15, 16, 17, 18, 19, 20]. The value of p corresponds to the fraction of conducting rock to total rock of the reservoir. This captures the essential features of the reservoir, while avoiding some of the non-crucial complications. An additional advantage to this approach is that it makes available to the analysis of oil recovery the wealth of information pertaining to percolation theory. However, we must caution the reader that these approximations cannot be taken as the definitive description for oil reservoirs. It is well known [21, 22, 23, 24, 25] that true field-size porous media possess correlations. Our description merely represents a first order approximation, which can serve as a base for more comprehensive studies.

To fully explain the flow of oil in a percolation cluster, several physical and geometric parameters of percolation have been explored. Among them, there is work on the shortest path in a percolation cluster [9, 11, 13, 35, 36, 37, 38, 39, 40, 41, 42], the average flow time of a fluid inside a cluster [43], and the full probability distribution of flow time inside a cluster for relatively short times [12]. The multifractal nature of flow inside a cluster has also been the subject of a number of articles [44, 45].

In this work, we focus on one particular technique of oil extraction used by companies: secondary oil extraction. It consists of injecting a fluid (water, carbon dioxide or methane) into the reservoir in order to displace the oil trapped inside. The fluid is injected through an injection well, located at point A of the reservoir, and the mixture of fluid and oil is collected at point B of the reservoir, where an extraction well is placed. The distance between the wells is known as the *interwell space* r. Inside the reservoir medium, a mixture of two fluids is formed, driven by a pressure difference between wells A and B. Here, we consider the case when the two fluids have equal viscosities and are both incompressible, and thus can be considered as identical miscible fluids. For fluids of different viscosities, see [49, 50, 46, 47, 48]. To predict the amount of oil obtained at a given time, one must understand the evolution of this flow. In particular, it is important to know how long the injected fluid starting at A requires to reach B. Since the flow on the reservoir occurs in the set of paths that connect A and B, knowledge of the *traveling time* t (also known in the literature as first-passage time) on all the paths in the reservoir determines how much of the displacing fluid has reached B at a given time and therefore, what percentage of the extracted mixture still corresponds to oil.

Some progress has been made in the study of this problem. The case of homogeneous flow (with $p = 1$), when the reservoir is only composed of conducting rock has been treated in [15]. Also, the convective and diffusive regimes of a more realistic non-homogeneous reservoir (specifically at criticality $p = p_c$) have been considered [12, 13, 15]. The time it takes for any amount of the injected fluid to reach B, called the breakthrough time $t_{\rm br}$, was analyzed in [12, 13]. The case of different viscosities for the injected and displaced fluids has been studied before, both for a finite value of the viscosity ratio [46, 47, 48], and in the limit of very high ratio [49, 50]. In the last case, a behavior analogous to diffusion-limited-aggregation (DLA) in percolation is found.

In this chapter, we analyze analytically and numerically the flow inside a 2-d bond percolation cluster for two different occupation probabilities ($p = 1$ and $p = p_c$) and under two different pumping conditions at A: constant current and constant pressure. The quantity measured is the probability distribution of the traveling time t of tracer particles after breakthrough in a percolation ensemble, for a given interwell space r, and a reservoir of linear dimension L. These measurements ultimately allow us to write the probability distributions in concise expressions, valid for all the conditions studied here.

In Sec. 2.3, we introduce the basic mathematical quantities, the probability density of traveling times and the production curve, and relate them to the physical picture. Sec. 2.4 deals with the homogeneous case $p = 1$, which serves as a template to understand the more complicated $0 < p < 1$ case. Sec. 2.5 introduces the inhomogeneous model at criticality to be used, while Sec. 2.6 recounts the numerical results of the model. In Sec. 2.7, we present analytical arguments explaining the behaviors observed in Sec. 2.6 and these arguments are then used to present the final forms for the probability distributions under both constant current and constant pressure conditions.

2.3 Preliminary concepts

In secondary oil extraction, a fluid (typically water) is injected into the reservoir through an injection or pumping well A, pushing oil trapped inside toward the extraction well B. We call any infinitesimal fluid element of water a *tracer*. The time it takes a tracer to travel from A to B is called the *traveling time* t. For each possible configuration of the reservoir, there are generally many possible paths to travel from A to B and each of these paths is called a *streamline*. Because of the multiplicity of streamlines, each particular tracer that starts at A, in general, requires a different time t to reach B. The breakthrough time $t_{\rm br}$ corresponds to the time when the first water stream reaches B for a given realization. We define $P(t, r, L)dt$ as the probability that a tracer crosses from A to B in a time between t and $t + dt$, with the condition that A and B are separated by a distance r, in a reservoir of linear size L. The function $P(t, r, L)$ is averaged over all possible reservoir configurations connecting the wells. Physically, it represents the fraction of water that *becomes* part of the extracted mixture at time t. Note that when $t < t_{\rm br}$, $P(t, r, L) = 0$, and the mixture corresponds to oil only. For $t \geq t_{\rm br}$, certain tracers begin to reach B, and $P(t, r, L) > 0$, giving a mixture of oil and water at B. As $t \to \infty$, $P(t, r, L) \to 0$, because no new streamlines reach B and this well produces only water. Cost constraints dictate the point at which the use of the well is terminated.

From our knowledge of $P(t, r, L)$, assuming that the streamlines do not change over time, we can determine the *average production curve* $C(t, r, L)$, which is the ratio of oil contained in the mixture coming out of the extraction well at time t

$$C(t,r,L) \equiv 1 - \int_0^t P(\tilde{t},r,L)d\tilde{t}. \tag{2.1}$$

Equation (2.1) exhibits the expected features of the mixture: initially $P(t,r,L) = 0$ and only oil comes out, giving $C(t,r,L) = 1$. As t increases, $C(t,r,L)$ begins to decay as a function of the number of streamlines that reach the extraction well. As $t \to \infty$, all water streamlines reach the extraction well and $C(t,r,L) = 0$.

For a reservoir being exploited with a pressure differential between A and B, such that the total current between these two points is Q, the total amount of oil S contained inside the reservoir can be determined by the expression

$$S = Q \int_0^\infty C(t)dt. \tag{2.2}$$

Assuming oil is incompressible and using units for which its density is equal to one, S also represents the accessible volume of the reservoir. Inserting Eq. (2.1) into Eq. (2.2) and integrating by parts, we obtain

$$\begin{aligned} \frac{S}{Q} &= \int_0^\infty dt(1 - \int_0^t P(\tilde{t},r,L)d\tilde{t}) \\ &= \int_0^\infty tP(t,r,L)dt \\ &= \langle t \rangle. \end{aligned} \tag{2.3}$$

This result corresponds to the *equal-time theorem*, which states that the average traveling time of tracers inside the reservoir is equal to the available reservoir volume divided by the total external current [15, 51]. Eq. (2.62) of Appendix 2.9 represents the same result, applied to a reservoir in which all the sand is conducting.

2.4 Homogeneous case

The homogeneous case ($p = 1$), which can be analytically solved, serves as a guide for the more realistic, non-analytic critical percolation threshold case ($p = p_c$). The $p = 1$

case was studied in [52] using differential equations. Here, we obtain the solutions by conformal mapping, reproducing the results of [52], and add the particular form of the production curve for the times t right after the breakthrough. This section contains the main results of the time behavior, but the derivations are located in Appendix 2.9. One of the results obtained there is that t carries units of r^2 and therefore, in the following, t is replaced by a scaled variable

$$t' \equiv \frac{t}{r^2}. \tag{2.4}$$

We assume that the reservoir is a circle of diameter L centered at the origin and the two points A and B are located at $(-r/2, 0)$ and $(r/2, 0)$. We study the production curve $C(t, r, L)$. The ratio L/r is represented by λ. Using t' and λ, the production curve $C(t, r, L)$ for a given r and L is

$$C(t', \lambda) \equiv C(t/r^2, 1, \lambda) = C(t, r, L), \tag{2.5}$$

where we have made use of Eq. (2.71), which expresses the scaling rule of $C(t, r, L)$ under rescaling of t to t/r^2. For the sake of brevity, we refer to $C(t', \lambda)$ as $C(t')$.

Originally, the reservoir is filled with one kind of fluid (oil). At time $t' = 0$, we start to inject at point A, with constant rate, a different fluid (water). We measure the production curve $C(t')$ at well B (Fig. 2.1). We assume that both fluids are incompressible and have zero viscosity. The flow is then described by Darcy's Law $\vec{v} = -\kappa \vec{\nabla} P$ and $\nabla^2 P = 0$. A set of regions, and two transition times $t'_{1/2}$ and t'_ℓ separating these regions, appears for the production curve $C(t')$. We now present them.

- **Region $\mathbf{I}_{\boldsymbol{H}}$.** Before $t' = t'_{\mathrm{br}}(\lambda)$, the concentration of injected fluid at point B is zero and only oil exits through point B. We denote this time region, when $t' \leq t'_{\mathrm{br}}$, as region I_H.

- **Region $\mathbf{II}_{\boldsymbol{H}}$.** When the injected fluid reaches the production well, the concentration of the displaced fluid rapidly drops immediately after breakthrough

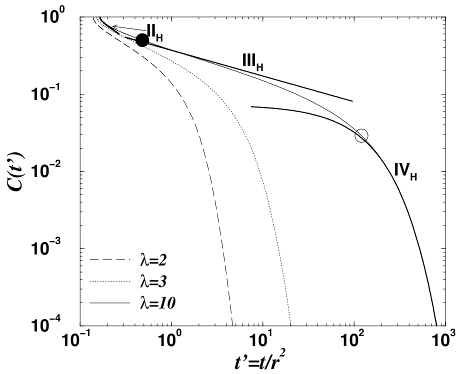

Figure 2.1: Production curves for the homogeneous $p = 1$ case in logarithmic scale for $\lambda = 2$, 3, and 10. The solid curves superimposed to the production curves indicate the asymptotic behaviors of regions II_H, III_H, and IV_H. All the solid lines have been calculated using the results in the Appendix 2.9. For region II_H, Eq. (2.69) is used with K given by Eq. (2.74); for region III_H, Eq. (2.70) is used and for region IV_H, we applied Eq.(2.79). The full circle indicates the transition time $t'_{1/2}$ and the empty circle indicates t'_ℓ.

as

$$C(t') \sim 1 - K(\lambda)\sqrt{t' - t'_{\mathrm{br}}}. \tag{2.6}$$

This behavior occurs until $t' = t'_{1/2}(\lambda)$, when a new time dependence sets in. The time region $t'_{\mathrm{br}} < t' \leq t'_{1/2}$ is defined as region II_H.

- **Region III_H.** If $\lambda \gg 1$, for times $t' > t'_{1/2}$ there exists a region of power law decay [52],

$$C(t') \sim t'^{-1/3}. \tag{2.7}$$

We call this region III_H. It is present at times $t'_{1/2} < t' \leq t'_\ell$, where $t'_\ell(\lambda)$ is defined below.

- **Region IV_H.** At the transition time $t'_\ell(\lambda)$, the reservoir is almost exhausted of oil and $C(t')$ decays exponentially as

$$C(t') \sim \exp(-(t' - t'_o)/t'_\ell), \tag{2.8}$$

where $t'_o(\lambda)$ is given by Eq. (2.78). This is region IV$_H$ and it is present in $C(t')$ for all $\lambda > 1$, for times $t' > t'_\ell$. For $\lambda = 1$, $C(t', 1) = 2C(2t', \infty) - 1$ and the reservoir is completely exhausted at $(1/2)t'_{1/2}(\infty)$.

- **Transition times $t'_{1/2}$ and t'_ℓ.** Regions II$_H$ and III$_H$ are separated by a transition or *crossover* time $t'_{1/2}(\lambda)$, given by Eq. (2.75). Regions III$_H$ and IV$_H$ are separated by the crossover time $t'_\ell(\lambda)$, given by Eq. (2.77). For $\lambda \sim 1$, the two crossover times become of the same order, and region III$_H$ is no longer present. However, as $\lambda \to \infty$

$$t'_{1/2}(\lambda) \to 1/2, \tag{2.9}$$

and [52]

$$t'_\ell(\lambda) \sim \lambda^{d_l} \qquad [d_l = 3]. \tag{2.10}$$

That is, as λ increases, region III$_H$ appears and the transition time between III$_H$ and IV$_H$ scales as a cubic function of the geometric factor λ.

2.5 Model for the inhomogeneous case

We represent the reservoir as a two-dimensional bond percolation cluster and choose points $(-r/2, 0)$ and $(r/2, 0)$, denoted by A and B, respectively, to be the injection and extraction well positions. Points A and B are separated by a geometric distance r and the system box has corners at $(\pm L/2, \pm L/2)$. We construct a percolation cluster by removing bonds of a square $L \times L$ lattice with probability $(1-p)$. Equivalently, each bond of the lattice is conducting with probability p and insulating with probability $1 - p$. We simulate the flow if the points A and B belong to the same conducting cluster. Otherwise, we discard the configuration. We restric our simulations to the critical bond percolation probability $p = p_c = 0.5$ [2]. We consider both spanning clusters and finite clusters, and perform averages over 10^4 realizations of the medium.

To model the flow of water, we use the analogy with electrical circuits, where for each bond, the pressure drop corresponds to the voltage difference and the flow corresponds to the electrical current on the bond. A pressure difference between points A and B drives the tracer. We choose the value of the pressure difference according to the conditions desired: for constant pressure, we set a pressure difference of 1 between A and B for all realizations of the medium; for constant current, we first measure the resistance R of the realization, and the pressure drop is chosen to be equal to R, so that the current for the realization is one. For each realization, 10^4 tracers are introduced at point A and then collected at point B. The set of all bonds with non-zero current contained in the percolation cluster for each particular realization defines the backbone of the cluster and the backbone mass M_B is the number of bonds that constitute this backbone.

Mathematically, the "pressure" difference across bonds is equivalent to a "voltage" difference, so by solving Kirchoff's laws on the backbone, we obtain the potential (pressure) drops ΔP over all bonds for a given realization. For a node having s outgoing bonds, the tracer selects a bond with a probability

$$w_{ij} = \frac{\Delta P_{ij}}{\sum_j \Delta P_{ij}} \qquad [j = 1, \ldots, s \text{ and } i = 1, \ldots, M_B]. \tag{2.11}$$

Here the index i is over the M_B nodes and j is over the s outgoing bonds, i.e., the bonds for which the pressure at the node i is larger than the pressure at the other node of the bond. For incoming bonds, $w_{ij} = 0$. The time necessary to cross each bond is $t_{ij} = 1/\Delta P_{ij}$ and the velocity is $v_{ij} = \Delta P_{ij}$ since each bond has unit length. The total traveling time of a tracer is the sum of the times corresponding to all the bonds of the path connecting A and B, chosen by this tracer. Since the particles do not interact with each other, it is equivalent to launching one particle at a time into the cluster. This procedure is known as *particle launching algorithm* [15, 53].

We determine the probability distribution of the traveling times $P(t, r, L)$ by counting the number of particles that travel from point A to point B, separated by a distance r in a box of linear size L, in a time between t and $t + dt$, over all the particles and all realizations of the medium simulated.

2.6 Results for the inhomogeneous case

Following earlier work [13], and in a similar way to Sec. 2.4, we define scaled times t_P and t_C to study the flow at both constant pressure and constant current conditions. For constant pressure, the scaled time is $t_P \equiv t/r^{d_B+\tilde{\mu}}$ and for constant current it is $t_C \equiv t/r^{d_B}$, where d_B is the backbone fractal dimension and $\tilde{\mu}$ is the characteristic exponent of the resistivity dependence on distance. The current values for these exponents are $d_B = 1.6432 \pm 0.0008$ and $\tilde{\mu} = 0.9826 \pm 0.0008$ [43, 54]. Under these new variables, we can define, in analogy to the homogeneous case (Eq. (2.5) and Eq. (2.71)), two new probability distributions

$$P(t_C, \lambda) \equiv P(t_C = t/r^{d_B}, 1, \lambda), \tag{2.12}$$

for constant current conditions and

$$P(t_P, \lambda) \equiv P(t_P = t/r^{d_B+\tilde{\mu}}, 1, \lambda), \tag{2.13}$$

for constant pressure. The functions $P(t_C, \lambda)$ and $P(t_P, \lambda)$ are independent of r and L, as reflected by the notation, but depend only on the ratio λ. Below, we refer to $P(t_P, \lambda)$ as $P(t_P)$ and to $P(t_C, \lambda)$ as $P(t_C)$, with the understanding that these functions are still dependent on λ. The two log-log plots Fig. 2.2(a) and Fig. 2.2(b) contain three simulations each, corresponding to the probability distributions $P(t_P)$ and $P(t_C)$ respectively; both plots were prepared using $\lambda = 32$ and system sizes $L = 258, 514, 1026$. The curves overlap in both the constant pressure and constant

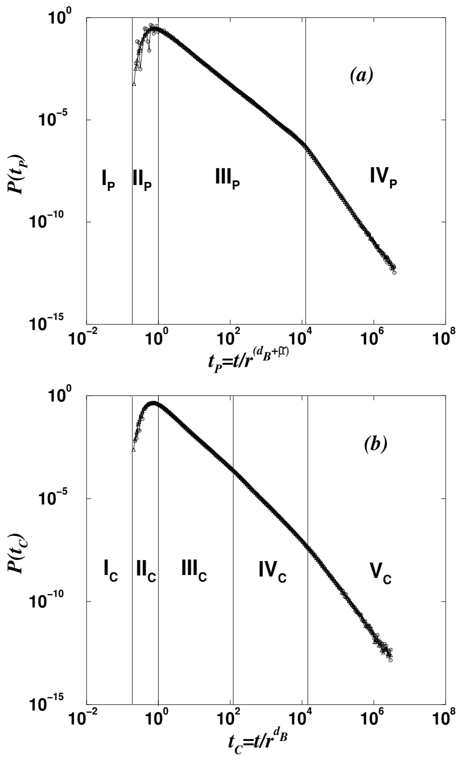

Figure 2.2: (a) Probability distribution of traveling times for constant pressure conditions for $\lambda = 32$. Three simulations are presented, for $L = 258, 514, 1026$. (b) Probability distribution of traveling times for constant current conditions for $\lambda = 32$. Three simulations are presented, for sizes $L = 258, 514, 1026$.

current cases, which imply the scaling properties

$$P(t_C, \lambda) = r^{d_B} P(t, r, L) \tag{2.14}$$

and

$$P(t_P, \lambda) = r^{d_B+\tilde{\mu}} P(t, r, L). \tag{2.15}$$

A set of regions with different behaviors appears in the two distributions. For the constant pressure distribution $P(t_P)$, we encounter:

- **Region I_P**, which corresponds to times smaller than the breakthrough time, before water reaches the extraction well;

- **Region II$_{\boldsymbol{P}}$**, appearing when the first water streams reach B and ending at the onset of a constant slope region, including the maximum of $P(t_P)$;

- **Region III$_{\boldsymbol{P}}$**, characterized by a constant value of the slope, defined as $-g_P^{(1)}$, of value -1.41 ± 0.01, and;

- **Region IV$_{\boldsymbol{P}}$**, which corresponds to another constant slope, defined as $-g_P^{(2)}$ and measured to be -2.43 ± 0.06.

The scaled crossover time from region III$_P$ to region IV$_P$ is called τ_P.

The results for the constant current distribution $P(t_C)$ are similar to those of constant pressure. However, there is a difference in that there is yet another constant slope region present. Consequently, we have:

- **Region I$_{\boldsymbol{C}}$**, for times before breakthrough;

- **Region II$_{\boldsymbol{C}}$**, corresponding to times right after breakthrough and until the first constant slope region appears, including the maximum of $P(t_C)$;

- **Region III$_{\boldsymbol{C}}$**, corresponding to a first slope, denoted by $-g_C^{(1)}$, of value -1.56 ± 0.01;

- **Region IV$_{\boldsymbol{C}}$**, for a second slope $-g_C^{(2)}$, with a value of -1.75 ± 0.01 for $\lambda = 32$, but with a heavy dependence with respect to λ and;

- **Region V$_{\boldsymbol{C}}$**, with a slope represented by $-g_C^{(3)}$, measured to be -2.45 ± 0.04.

The scaled crossover time between III$_C$ and IV$_C$ is defined as $\tau_C^{(1)}$ and between IV$_C$ and V$_C$, as $\tau_C^{(2)}$. All these values are presented in Table 2.1.

Next, we present simulations for the probability distributions of traveling times for both constant current and constant pressure and for *different* λ values (Fig. 2.3). As before, the distributions have two constant slope decay regions for constant pressure and three for constant current. However, as λ changes, the positions of these regions

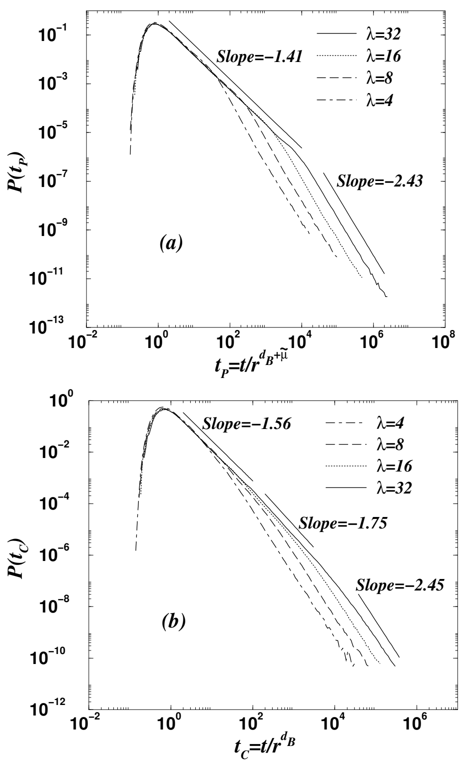

Figure 2.3: (a) Probability distribution of traveling times for constant pressure conditions for system size $L = 514$. Four simulations are presented, for $\lambda = 4, 8, 16, 32$. (b) Probability distribution of traveling times for constant current conditions for system size $L = 514$. Four simulations are presented, for $\lambda = 4, 8, 16, 32$.

change as well. The detailed shapes of $P(t_P)$ and $P(t_C)$ can be determined by studying their successive slopes, shown for constant pressure conditions in Fig. 2.4(a), and for constant current in Fig. 2.4(b). It is noteworthy that regions III_C and IV_C become shorter as λ decreases, with region III_C disappearing for $\lambda \leq 4$, and region IV_C for $\lambda \leq 2$.

Another set of quantities studied are the times for which the slopes crossover between regions. These crossover times are indicated by ellipses and boxes in Fig. 2.4(a) and Fig. 2.4(b). For the case of constant pressure, Fig. 2.5 shows the scaling of the crossover time τ_P with respect to λ, found to be $\tau_P \sim \lambda^{d_P}$ with $d_P = 2.78 \pm 0.15$.

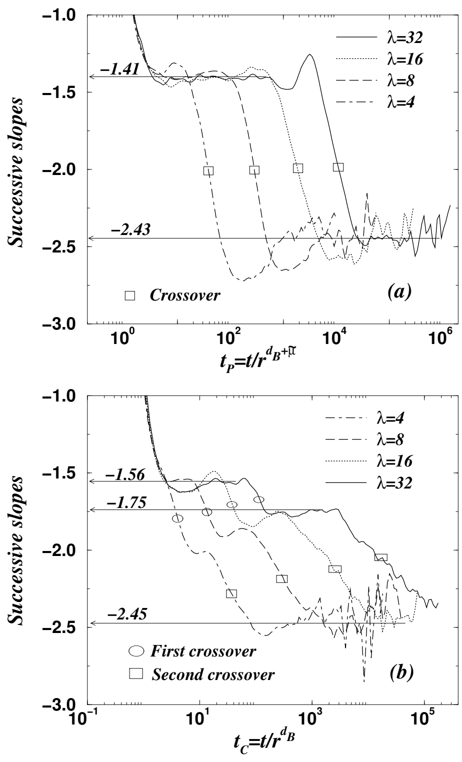

Figure 2.4: (a) Successive slopes for the probability distribution of traveling times for constant pressure conditions for system size $L = 514$ (shown in Fig. 2.3). Four simulations are presented, for $\lambda = 4, 8, 16, 32$. (b) Successive slopes for the probability distribution of traveling times for constant current conditions for system size $L = 514$. Four simulations are presented, for $\lambda = 4, 8, 16, 32$.

For constant current, Figs. 2.6(a) and 2.6(b) show two crossover times $\tau_C^{(1)}$ and $\tau_C^{(2)}$, which scale as $\tau_C^{(1)} \sim \lambda^{d_C^{(1)}}$ and $\tau_C^{(2)} \sim \lambda^{d_C^{(2)}}$ with $d_C^{(1)} = 1.74 \pm 0.05$ and $d_C^{(2)} = 2.90 \pm 0.09$, respectively. The positions of the crossover times have been determined by finding the positions of the inflection points of the successive slopes plots.

Of practical interest is the production curve for constant current conditions (Fig. 2.7), because it supplies a tool for estimating the oil production efficiency. This curve is obtained by using Eq. (2.1), from the probability distribution of $P(t_C)$ (shown in Fig. 2.3b).

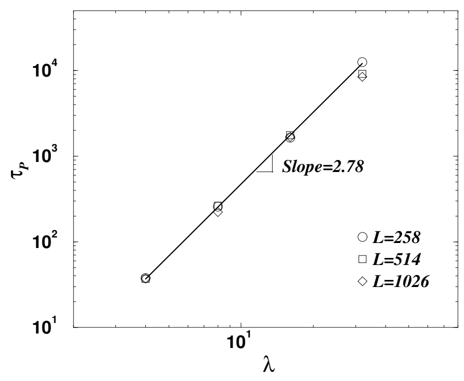

Figure 2.5: Crossover times from region III$_P$ to region IV$_P$ for constant pressure conditions, with a system size of $L = 258, 514, 1026$ and $\lambda = 4, 8, 16, 32$.

2.7 Discussion

The distributions of traveling time under constant current and constant pressure conditions are connected to one another. By definition, $t_P = (\tilde{R}/r^{\tilde{\mu}})t_C$, with $\tilde{R}$ being the resistance of a percolation cluster [2, 5], which is defined operationally as the voltage obtained between points A and B when a current of value 1 is present. The probability that a percolation cluster at the critical concentration p_c has resistance $\tilde{R}$ is given by $\tilde{\Phi}(\tilde{R})d\tilde{R}$, and can be seen in Fig. 2.8. Approximately, $\tilde{\Phi}(\tilde{R})$ is given by

$$\tilde{\Phi}(\tilde{R}) \sim \begin{cases} 0 & \tilde{R} \leq \tilde{R}_{min} \\ \tilde{R}^{-g_R} & \tilde{R}_{min} < \tilde{R} \leq \tilde{R}_{max} \qquad [g_R = 2.10 \pm 0.20] \\ 0 & \tilde{R} > \tilde{R}_{max}, \end{cases} \tag{2.16}$$

with $\tilde{R}_{min} \sim r^{\tilde{\mu}}$ and $\tilde{R}_{max} \sim L^{\tilde{\mu}}$. The labels for $\tilde{R}_{min}$ as minimum resistance, and for $\tilde{R}_{max}$ as maximum resistance, reflect the scaling rules of $\tilde{R}$ with respect to the linear size x of a cluster, i.e., $\tilde{R} \sim x^{\tilde{\mu}}$ [2]. Therefore, since the interwell distance is r, the $r^{\tilde{\mu}}$ represents the typical minimum value of resistance $\tilde{R}_{\min}$. The maximum resistance becomes determined by the system size and it scales as $L^{\tilde{\mu}}$. The function $\tilde{\Phi}(\tilde{R})$ is not strictly zero for $\tilde{R} \leq \tilde{R}_{min}$ or $\tilde{R} > \tilde{R}_{max}$, but this is an acceptable approximation in

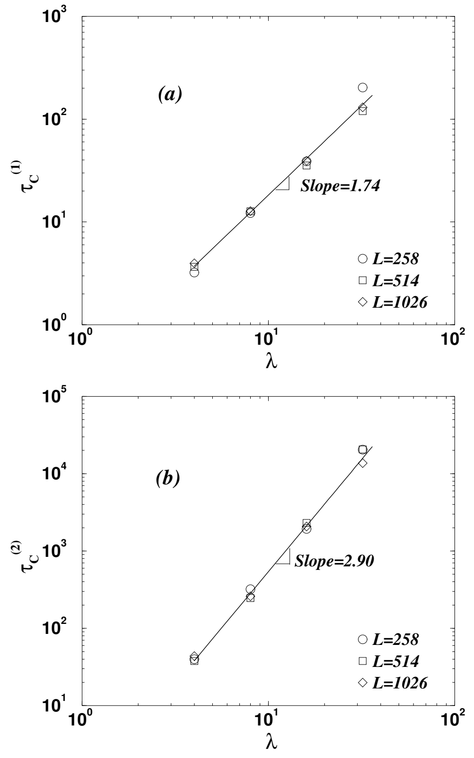

Figure 2.6: (a) Crossover times from region III_C to region IV_C for constant current conditions, with system sizes $L = 258, 514, 1026$. (b) Crossover times from region IV_C to region V_C for constant current conditions, with system sizes $L = 258, 514, 1026$.

our theory. All the results we present for $\Phi(\tilde{R})$ are in agreement with previous work [13, 55].

As with the rescaled times, we find it convenient to define a scaled resistance $R = \tilde{R}/r^{\tilde{\mu}}$ [13] and an associated probability $\Phi(R) \equiv r^{\tilde{\mu}}\tilde{\Phi}(\tilde{R} = Rr^{\tilde{\mu}})$. The function $\Phi(R)$ obeys the same scaling as $\tilde{\Phi}(\tilde{R})$ (it satisfies Eq. (2.16) dropping the tilde sign). The quantity $R_{min} \equiv \tilde{R}_{min}/r^{\tilde{\mu}}$ now becomes geometry independent and $R_{max} \equiv \tilde{R}_{max}/r^{\tilde{\mu}}$ scales as $R_{max} \sim \lambda^{\tilde{\mu}}$.

The redefined resistance R reduces the relation between t_P and t_C to $t_P = Rt_C$.

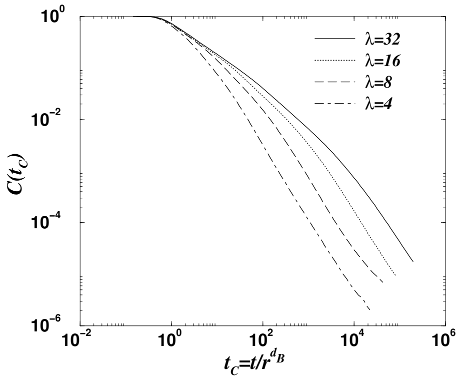

Figure 2.7: Production curve for system size $L = 1026$, under constant current conditions. Four interwell distances have been used, for $\lambda = 4, 8, 16, 32$.

Thus, $P(t_P|R)$ and $P(t_C|R)$ are related by $P(t_C|R)dt_C = P(t_P|R)dt_P$ and give

$$P(t_C|R) = RP(t_P|R). \tag{2.17}$$

Hence, knowledge of one distribution enables us to calculate the other.

We focus on $P(t_P)$ initially. We consider the parameter R, the scaled resistance of the cluster, as the relevant physical quantity dominating the properties of $P(t_P)$. Therefore, we numerically find $P(t_P|R)dt_P$, which corresponds to the probability that a tracer particle travels between points A and B in a cluster with resistance R (more formally, with resistance within the range R to $R + dR$). The function $P(t_P)$ can be constructed by the convolution

$$P(t_P) = \int P(t_P|R)\Phi(R)dR. \tag{2.18}$$

The function $P(t_P|R)$, seen in Fig. 2.9, is obtained from the simulation of a system with $L = 1026$ and $r = 32$, or equivalently, with $\lambda = 32$. Each curve represents a different value of the resistance R. The detailed behavior of the $P(t_P|R)$ has several features. The function reaches a maximum at time

$$t_P^* \sim R^{d_R} \qquad [d_R = 2.57 \pm 0.02], \tag{2.19}$$

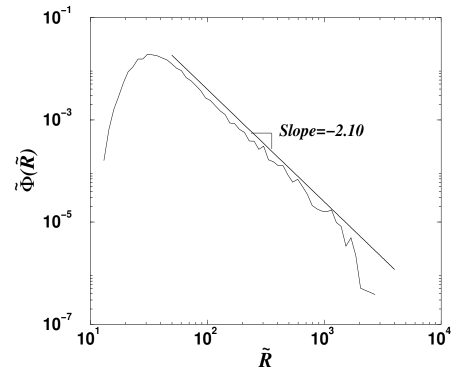

Figure 2.8: Probability density $\tilde{\Phi}(\tilde{R})$ vs. $\tilde{R}$ for a simulation with system size $L = 1026$ and $\lambda = 32$.

as seen in Fig. 2.11. The scaled crossover time between the two power law regions in Fig. 2.9, defined by the notation $t_P^{\times}$, occurs at equal time for all the curves, which indicates that it is independent of the resistance R. However, we have performed other simulations with different values of λ, and have found that

$$t_P^{\times} \sim \lambda^{d_\times} \qquad [d_\times = 2.84 \pm 0.10]. \tag{2.20}$$

The region $t_P^* \leq t_P < t_P^{\times}$ is characterized by a power law decay of changing slope $-\gamma^{(1)}$ in the log-log plot (Fig. 2.9). For times t_P close to t_P^*, the slope presents a value close to -2, and as $t_P \to t_P^{\times}$, the value gradually changes to -1.6 (see Fig. 2.10). Additionally, as becomes apparent in Sec. 2.7.5, $\gamma^{(1)}$ is also λ dependent, a fact that affects the value of the exponent $g_C^{(2)}$. We do not have a satisfactory explanation for this time dependence of $\gamma^{(1)}$, but as a first order approximation, in what follows we assume it to be a constant, of value $\gamma^{(1)} = 1.74 \pm 0.15$, with the value given by its average over the range $t_P^* \leq t_P < t_P^{\times}$. The second region in Fig. 2.9, for times $t_P \geq t_P^{\times}$, is characterized by a slope of value $\gamma^{(2)} = 2.41 \pm 0.04$. In analytical form, $P(t_P|R)$

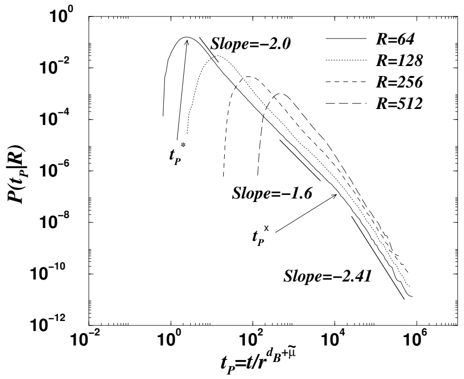

Figure 2.9: Probability distribution $P(t_P|R)$ vs. $t_P = t/r^{d_B+\tilde{\mu}}$ for system size $L = 1026$ and interwell spacing $r = 32$ ($\lambda = 32$), under constant pressure conditions. The most probable traveling time t_P^* and the crossover time $t_P^\times$ are indicated for the curve corresponding to $R = 64$.

can be approximated as

$$P(t_P|R) \sim \begin{cases} 0 & t_P < t_P^* \\ t_P^{-\gamma^{(1)}} & t_P^* < t_P < t_P^\times \qquad [\gamma^{(1)} = 1.74 \pm 0.15] \\ t_P^{-\gamma^{(2)}} & t_P > t_P^\times \qquad [\gamma^{(2)} = 2.41 \pm 0.04]. \end{cases} \tag{2.21}$$

Taking $P(t_P|R)$ to be identical to zero for $t_P < t_P^*$, although an approximation, simplifies our calculations considerably and does not affect the validity of our results. In fact, this is a very good approximation since there are very few tracers reaching well B in this time range, which means that their statistical contribution is negligible. This simplifying assumption is repeated below for $P(t_C|R)$. The actual behavior of $P(t_P|R)$ for $t_P < t_P^*$ has been studied in detail before [13], where it was found to be that of a stretched exponential, carrying negligible statistical weight in our present calculations. In Sec. 2.7.5, we incorporate this result into the full scaling *ansatz* for $P(t_P)$ and $P(t_C)$. The numerical values of the exponents of $P(t_P|R)$ and $\Phi(R)$ are summarized in Table 2.2.

The similarity in the values of d_R and the combination $1 + d_B/\tilde{\mu}$ is worth some

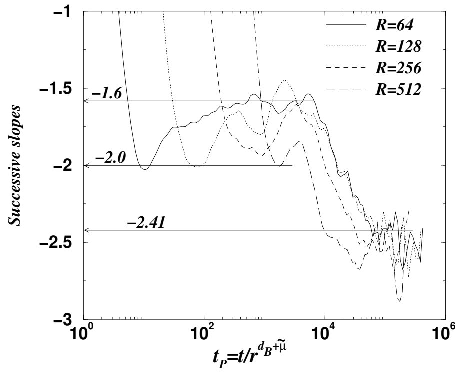

Figure 2.10: Successive slopes for $P(t_P|R)$, with a system size $L = 1026$ and $\lambda = 32$. The region corresponding to slope $\gamma^{(1)}$ of $P(t_P|R)$ varies in value, as indicated by the horizontal lines, between -1.60 and -2.00. The second slope $\gamma^{(2)}$ reflects a more constant behavior, with value 2.41 ± 0.04.

consideration. It has been proposed elsewhere [12] that under constant current conditions, the unscaled most probable traveling time scales with respect to r as r^{d_B}. Now, for a fixed value of the resistance R, at constant pressure conditions ($t_P = Rt_C$), we expect the unscaled most probable traveling time to scale as $r^{d_B+\tilde{\mu}}$, where the scaling rule $\tilde{R} = Rr^{\tilde{\mu}}$ has been used. These considerations justify our choice of rescaled times. Since $\tilde{R} \sim r^{\tilde{\mu}}$, we can assume that the most probable traveling time at constant $\tilde{R}$ scales as $\tilde{R}^{1+d_B/\tilde{\mu}}$ and thus, $d_R = d_B/\tilde{\mu} + 1$. By similar arguments regarding the longest possible tracer trajectories inside the system, the unscaled crossover time can be related to $L^{d_B+\tilde{\mu}}$, indicating that $t_P^{\times} \sim \lambda^{d_\times}$ would have $d_\times$ be equivalent to $d_B + \tilde{\mu}$. However, our numerical simulations do not have sufficient accuracy to answer these question definitively.

The properties just described for $P(t_P|R)$ and use of Eq. (2.18), determine the form of $P(t_P)$ as we now prove for each separate region identified in Figs. 2.2(a) and 2.2(b) (see also Sec. 2.6). The analytical expressions for all the predicted exponents pertaining to the distribution $P(t_P)$ and their numerical values are given in Table 2.1.

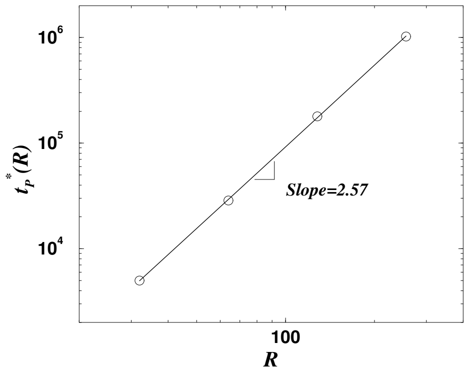

Figure 2.11: Scaling of the maximum $t_P^*(R)$ of the probability $P(t_P|R)$ vs. the resistance R, for a system size $L = 1026$, and interwell distance $r = 32$ ($\lambda = 32$). The quantity $t_P^*(R)$ scales with R as R^{d_R}, with $d_R = 2.57 \pm 0.02$

2.7.1 Region III$_P$

To use $P(t_P|R)$ for the calculation of $P(t_P, \lambda)$, according to Eq. (2.18), we need to take into account its normalization factor, which is R dependent. To obtain this factor, we integrate the distribution and equate it to unity, using the following assumptions: $P(t_P|R)$ is strictly equal to zero for times $t_P < t_P^* \sim R^{d_R}$ and, as a consequence of the previous condition, the lower limit of integration is $t_P^* \sim R^{d_R}$. The final form of $P(t_P|R)$ is

$$P(t_P|R) \sim \begin{cases} 0 & t_P < t_P^* \\ \frac{1}{R^{d_R}}\left(\frac{t_P}{R^{d_R}}\right)^{-\gamma^{(1)}} & t_P^* < t_P < t_P^{\times} \qquad [\gamma^{(1)} = 1.74 \pm 0.15] \\ \frac{R^{d_R(\gamma^{(1)}-\gamma^{(2)})}}{R^{d_R}}\left(\frac{t_P}{R^{d_R}}\right)^{-\gamma^{(2)}} & t_P > t_P^{\times} \qquad [\gamma^{(2)} = 2.41 \pm 0.04]. \end{cases} \tag{2.22}$$

Regarding $\Phi(R)$, its normalization has no impact on the variables in which we are interested and is therefore not presented.

To perform the integration of Eq. (2.18), we must first define the limits of integration in R that apply for region III$_P$. The R dependence of function $P(t_P|R)$ is contained in its normalization factor, and also in the fact that this distribution is non-zero when $t_P > t_P^* \sim R^{d_R}$. Therefore, for a given time t_P, the integrand of Eq. (2.18) is non-zero for all $R < t_P^{1/d_R}$. The lower limit of the integral is $R_{\min}$, but it is irrelevant with regards to the t_P scaling form. For the function $P(t_P|R)$, only the first scaling $t_P^{-\gamma^{(1)}}$ is used, since region III$_P$ is limited to $t_P \leq t_P^\times$. Then, using Eq. (2.16), Eq. (2.22), and the convolution Eq. (2.18), we obtain

$$P(t_P) \sim t_P^{-\gamma^{(1)}} \int^{t_P^{1/d_R}} R^{-d_R(-\gamma^{(1)}+1)} R^{-g_R} dR \tag{2.23}$$

for $t_P \leq t_P^\times$. After integration, the exponent of t_P is positive, which implies that the leading term for the integral is the upper limit of integration. Substituting this limit yields the scaling form $t_P^{(1-d_R-g_R)/d_R}$. Therefore, since in region III$_P$ the scaling is $P(t_P) \sim t_P^{-g_P^{(1)}}$, we obtain

$$g_P^{(1)} = \frac{g_R + d_R - 1}{d_R}. \tag{2.24}$$

2.7.2 Region IV$_P$ and crossover time τ_P

For times $t_P > t_P^\times$, the distribution $P(t_P|R)$, regardless of the value of R, decays with a power law of $t_P^{-\gamma^{(2)}}$. The upper limit of integration is determined by the largest resistance possible within the conditions of the geometry, which we denote by $R_{\max}$, and it is independent of t_P. Therefore, by convolution Eq. (2.18), we obtain

$$P(t_P) \sim t_P^{-g_P^{(2)}} = t_P^{-\gamma^{(2)}}, \tag{2.25}$$

giving

$$g_P^{(2)} = \gamma^{(2)}. \tag{2.26}$$

The actual numerical value of $g_P^{(2)}$ is discussed in Sec. 2.7.4.

The crossover time $t_P^\times$ separates regions III$_P$ and IV$_P$. Therefore, $\tau_P = t_P^\times$, which implies that

$$\tau_P \sim \lambda^{d_\times} \tag{2.27}$$

and

$$d_P = d_\times. \tag{2.28}$$

2.7.3 Mapping between $P(t_P)$ and $P(t_C)$

Based on Eq. (2.17), the differences observed in the curves for $P(t_P)$ and $P(t_C)$ are caused by a shift of the curve $P(t_P|R)$ on a log-log plot by $\log(1/R)$. The function $P(t_C|R)$, defined from $P(t_P|R)$ by Eq. (2.17), is characterized by two power law decays with exponents $-\gamma^{(1)}$ and $-\gamma^{(2)}$, a maximum at time $t_C^* \equiv t_P^*/R \sim R^{d_R-1}$, and a scaled crossover time between the two power law regions at $t_C^\times \equiv t_P^\times/R \sim R^{-1}t_P^\times$. In analytical form, $P(t_C|R)$ can be approximated by an equation similar to Eq. (2.22)

$$P(t_C|R) \sim \begin{cases} 0 & t_C < t_C^* \\ \frac{1}{R^{d_R-1}}\left(\frac{t_C}{R^{d_R-1}}\right)^{-\gamma^{(1)}} & t_C^* < t_C < t_C^\times \qquad [\gamma^{(1)} = 1.74 \pm 0.15] \\ \frac{R^{d_R(\gamma^{(1)}-\gamma^{(2)})}}{R^{d_R-1}}\left(\frac{t_C}{R^{d_R-1}}\right)^{-\gamma^{(2)}} & t_C > t_C^\times \qquad [\gamma^{(2)} = 2.41 \pm 0.04], \end{cases} \tag{2.29}$$

where the normalization factor has been obtained by assumptions analogous to those used for $P(t_P|R)$. To explain the different power law regions in the behavior of $P(t_C)$ we use the convolution

$$P(t_C) = \int P(t_C|R)\Phi(R)dR = \int P(t_P|R)R\Phi(R)dR, \tag{2.30}$$

where Eq. (2.17) has been taken into account.

In Eq. (2.29), the times t_C^* and $t_C^\times$ are dependent on R and therefore, the size of the scaling region $P(t_C|R) \sim t_C^{-\gamma^{(1)}}$ is R dependent as well. This is an important difference between the constant current and constant pressure cases, because it is the cause of the existence of regions III_C and IV_C with exponents that differ from each other and from the exponent of region III_P. The R dependence of the size of the region is as follows: as R increases, t_C^* increases, but $t_C^\times$ decreases. For large enough R, denoted here by $R_\times$, these two times coincide, and only the scaling $t_C^{-\gamma^{(2)}}$ is present. The resistance $R_\times$ scales as a function of the crossover time $t_P^\times$ as $R_\times \sim (t_P^\times)^{1/d_R}$ and ultimately, in terms of λ as $R_\times \sim \lambda^{d_\times/d_R}$. Also, there is a specific time, denoted here by M, associated with this point of coincidence, where only the power law decay with $t_C^{-\gamma^{(2)}}$ survives. Inserting $R_\times$ into $t_C^* \sim R^{d_R-1}$ (or alternatively into $t_C^\times \sim R^{-1}t_P^\times$), we obtain

$$M \sim \lambda^{(d_R-1)d_\times/d_R}. \tag{2.31}$$

It is now possible to explain the existence of regions III$_C$ and IV$_C$. For times $t_C < M$, the convolution integral in Eq. (2.30) has an upper limit obtained by the relation $t_C \sim R^{d_R-1}$ and consequently, the expression becomes

$$P(t_C) \sim t_C^{-\gamma^{(1)}} \int^{t_C^{1/(d_R-1)}} R^{-(d_R-1)+\gamma^{(1)}(d_R-1)-g_R} dR. \tag{2.32}$$

If the exponent of t_C after integration is positive, only the upper limit is relevant and the integral yields $P(t_C) \sim t_C^{(2-d_R-g_R)/(d_R-1)}$. Otherwise, the integral is finite and $P(t_C) \sim t_C^{-\gamma^{(1)}}$. For region III$_C$, the scaling behavior is $P(t_C) \sim t_C^{-g_C^{(1)}}$, implying that

$$g_C^{(1)} = min\left\{\frac{d_R + g_R - 2}{d_R - 1}, \gamma^{(1)}\right\}. \tag{2.33}$$

The predicted value for $g_C^{(1)}$ is different than the measured quantity, although it is within the error bars. This discrepancy is associated with the simplifications made in our theory, which do not reflect the fact that for $t_C < N$, the highest contribution to $P(t_C)$ comes from lower values of R, and $\Phi(R)$ in this range decays with an exponent g_R smaller than 2.1 (note the rounded shape of $\Phi(R)$ near its peak in Fig. 2.8). Therefore, with a smaller effective value of g_R, the exponent $g_C^{(1)}$ acquires a smaller value as well.

As it follows from the behavior of $P(t_P|R)$, for times $t_C > M$, $P(t_C|R)$ scales as $t_C^{-\gamma^{(1)}}$ for small values of R and as $t_C^{-\gamma^{(2)}}$ for larger R. The transition between the two situations occurs when $t_C = t_C^\times$, and since this last quantity scales as R^{-1}, then $t_C \sim R^{-1}$ and the upper limit of the integral for the regime $t_C^{-\gamma^{(1)}}$ is $R \sim t_C^{-1}$. Therefore, the convolution Eq. (2.30) is written as

$$P(t_C) \sim t_C^{-\gamma^{(1)}} \int^{t_C^{-1}} R^{-(d_R-1)+\gamma^{(1)}(d_R-1)-g_R} dR + t_C^{-\gamma^{(2)}} \int_{t_C^{-1}}^{R_{\max}} R^{-(d_R-1)+\gamma^{(1)}d_R-\gamma^{(2)}-g_R} dR. \tag{2.34}$$

Once again, by considering the value of the exponents after integration, given that $P(t_C) \sim t_C^{-g_C^{(2)}}$, we obtain for region IV_C

$$g_C^{(2)} = \min\{(\gamma^{(1)} - 1)d_R - g_R + 2, \gamma^{(1)}\}. \tag{2.35}$$

This result is valid for a given value of λ due to the dependence of $\gamma^{(1)}$ on this parameter. At the limit of very large λ, application of the equal-time theorem indicates that $g_C^{(2)}$ approaches $g_C^{(1)}$, or

$$g_C^{(2)} \to g_C^{(1)} \qquad [\lambda \to \infty], \tag{2.36}$$

which corresponds to Eq. (2.59). See Sec. 2.7.5 for details.

Because $t_C^{\times} \sim R^{-1}$, as R decreases, $t_C^{\times}$ increases. Consequently, the transition of $P(t_C|R)$ to the scaling $P(t_C|R) \sim t_C^{-\gamma^{(2)}}$ occurs at later times for smaller R. Since the minimum R possible is $R_{\min}$, the crossover $t_C^{\times}$ has an upper bound, denoted here by N. The form of N is determined through $P(t_C|R = R_{\min})$ and it is equal to $t_C^{\times}$ for this particular distribution, or

$$N \sim t_C^{\times} \sim R_{\min}^{-1} t_P^{\times} \sim \lambda^{d_\times}. \tag{2.37}$$

For $t_C > N$, we have $P(t_C|R) \sim t_C^{-\gamma^{(2)}}$. Using this form of $P(t_C|R)$ in the convolution Eq. (2.30) we obtain $P(t_C) \sim t_C^{-\gamma^{(2)}}$. The upper limit of integration is again $R_{\max}$. Thus, for region V_C, we have

$$g_C^{(3)} = \gamma^{(2)}. \tag{2.38}$$

This exponent is equal to that obtained for region IV_P.

Now we derive the expression for the first crossover time M, which separates regions III_C and IV_C. According to Eq. (2.31)

$$\tau_C^{(1)} = M \sim \lambda^{d_\times (d_R - 1)/d_R}. \tag{2.39}$$

Comparing this with the definition for $\tau_C^{(1)}$ given in Sec. 2.6, we obtain

$$d_C^{(1)} = d_\times (d_R - 1)/d_R. \tag{2.40}$$

The second crossover, according to Eq. (2.37), occurs at $\tau_C^{(2)} = N$ and obeys the scaling

$$\tau_C^{(2)} \sim \lambda^{d_\times}, \tag{2.41}$$

which in turn implies that

$$d_C^{(2)} = d_\times. \tag{2.42}$$

2.7.4 Long time regime for constant pressure and constant current

As a first approximation, we can assume that the functions $P(t_P)$ and $P(t_C)$, for a given ratio λ, have no dependence on the system size L. However, our numerical simulations suggest a weak dependence of the exponents $g_P^{(2)}$ and $g_C^{(3)}$ on the system size L. These exponents express only the long time behavior (large t_P and t_C or alternatively, regions IV$_P$ and V$_C$) of the distributions. The values of these exponents were found to be the same, since both $g_P^{(2)}$ and $g_C^{(3)}$ are equal to $\gamma^{(2)}$. Consequently, this means that $\gamma^{(2)}$ is a function of L. Based on the multifractal nature of flow in porous media [44] and particularly, on the results obtained in Ref. [45, 56], we propose an argument on how $\gamma^{(2)}$ depends on L. Since the scaling forms for $P(t_C)$ and $P(t_P)$ are the same at long times (regions IV$_P$ and V$_C$), for the rest of this section we introduce the notation $\tilde{t}$ to represent both t_P and t_C, because the following argument applies to both distributions.

Barthélémy et al. [45] studied the nature of the distribution of tracer velocities $\{v_i\}$ in a cluster connecting two points in percolation and found that it has multifractal properties. Particularly, $\tilde{P}(v_i) \sim v_i^{-1+a/\log_{10} L}$, where v_i is the velocity of the tracer through bond i, and a is a constant. What is the consequence of this distribution in terms of our problem? From the rules of the simulation, we have $\tilde{t}_i = 1/v_i$ and therefore, the distributions of both time and velocity are related by $\tilde{P}(v_i)dv_i = \tilde{P}(\tilde{t}_i)d\tilde{t}_i$. If a tracer travels through a bond with a velocity v_i that is among the lowest velocities on the realization, then it is true that $\tilde{t} \approx \tilde{t}_i$ i.e., the total time of the tracer is approximately equal to the time it takes to pass the slowest bond. Then $\tilde{P}(\tilde{t}) \approx \tilde{P}(\tilde{t}_i)$ and

$$\tilde{P}(\tilde{t}) \approx \tilde{P}(\tilde{t}_i) = \tilde{P}(v_i)\frac{dv_i}{d\tilde{t}_i}. \tag{2.43}$$

Given that the tracers choose to travel through a particular bond with a probability *proportional* to the value of the velocity in that bond, we then have to modify the distribution $\tilde{P}(v_i)$ for $v_i\tilde{P}(v_i)$ to take this into account. Therefore, we obtain a new distribution $P(v_i) \equiv v_i\tilde{P}(v_i)$, which equals $P(v_i) = v_i^{a/\log_{10} L}$. The corresponding time distribution to $P(v_i)$ is called $P(\tilde{t}_i)$ and satisfies

$$P(\tilde{t}_i) = v_i\tilde{P}(v_i)\frac{dv_i}{d\tilde{t}_i} = v_i^{a/\log_{10} L}\frac{1}{\tilde{t}_i^2} = \tilde{t}^{-2-a/\log_{10} L}. \tag{2.44}$$

Since we are treating the case for $\tilde{t} \approx \tilde{t}_i$, $P(\tilde{t}) = P(\tilde{t}_i)$. The probability distribution $P(\tilde{t})$ is the distribution satisfied for very large $\tilde{t}$ in our problem, which means that $P(\tilde{t}) \sim \tilde{t}^{-\gamma^{(2)}}$, or

$$\gamma^{(2)} = 2 + a/\log_{10} L. \tag{2.45}$$

In Fig. 2.12, we find the value of $\gamma^{(2)}$ as a function of $1/\log_{10} L$, measured from simulations, for several values of the ratio λ. Data regression for these results yields the expression

$$\gamma^{(2)} = 2.08 + 0.81\frac{1}{\log_{10} L}. \tag{2.46}$$

The agreement between the predicted and the empirical results suggests that we have reached a regime where the traveling time values are dominated by the times on these bonds. This regime starts for times τ_P at constant pressure and $\tau_C^{(2)}$ at constant current. These times, in turn, scale with λ with exponents $d_P = 2.78 \pm 0.15$ and $d_C^{(2)} = 2.90 \pm 0.09$, which are close to each other and to the quantities $d_\times$ and $d_B + \tilde{\mu}$. This scaling is consistent with the hypothesis that the long time regime appears when most of the fluid inside the cluster has been displaced and only the slowest parts of the cluster still preserve some original fluid. Since there are only two stagnation points

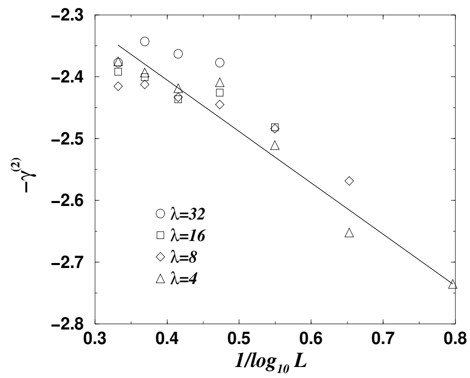

Figure 2.12: Value of the tail exponent $-\gamma^{(2)}$ as a function of $1/\log_{10} L$, where L corresponds to the system size of the simulation. Each symbol represents the succession of values of $\gamma^{(2)}$ for a given ratio λ, with the longest curve corresponding to ratio 4 and the shortest to ratio 32. The thick straight line represents the least squares fit of the $\lambda = 4$ case, which yields a line of value $\gamma^{(2)} = 2.08 + 0.81/\log_{10} L$, as stated in the text.

for the homogeneous case of Sec. 2.4, $P(t')$ is characterized by an exponential decay. This is in contrast to the $p = p_c$ case where a multifractal spectrum of stagnation points is present, generating a power law for $P(t')$. However, the long-time regime of the homogeneous case emerges in a time that scales as λ^{d_l}, with $d_l = 3$, and since at $p = 1$, $d_B = 2$ and $\tilde{\mu} = 1$, this becomes consistent with our picture.

It is important to point out that the power law behavior that we observe implies that the k-moments $\langle \tilde{t}_C^k \rangle$ of the distribution $P(t_C)$ (and the equivalent for $P(t_P)$) diverge for all sufficiently large k. This appears to be in contrast with earlier work [15], where the high current limit $Q \to \infty$ has finite moments for all k in a finite system. However, this apparent discrepancy is in fact due to the different conditions that are being considered. In [15], both convective and diffusive effects are present, and all tracers on a system are able to travel and eventually leave, even from very slow bonds, making the effect of the stagnation points negligible, and generating an exponential decay for the traveling time probability distribution. On the other hand, if no diffusion is present, as it is the case here, the presence of the multifractal distribution of the velocities of in the bonds generates a power law tail that makes the moments divergent; the tracers cannot *diffuse* away from the stagnation points.

2.7.5 The full scaling forms of $P(t_P)$ and $P(t_C)$.

The results obtained in Secs. 2.6 and 2.7 allow us to write a full set of scaling *ansatz* for the traveling time probability distributions under both constant current and constant pressure conditions. The *ansatz* takes into account the regions present in each of the distributions, as well as the short time cutoff (before $t' = t'_{\rm br}$). For the cutoff, we follow closely the arguments presented in [13], where this behavior is accounted for by the use of a stretched exponential function.

For constant pressure, we write

$$P(t_P) \sim t_P^{-g_P^{(1)}} F_P(t_P) G\left(\frac{t_P}{\lambda^{d_P}}\right), \tag{2.47}$$

where the functions $F_P(x)$ and $G(x)$ have the behaviors

$$F_P(x) \sim \exp(-bx^{-\phi}), \tag{2.48}$$

and

$$G(x) \sim \begin{cases} const. & x \ll 1 \\ x^{-g_P^{(2)}+g_P^{(1)}} & x \gg 1, \end{cases} \tag{2.49}$$

and the constants b and ϕ are fitted by the data. For ϕ, the data extracted from Fig. 2.2(a) yield $\phi = -1.42 \pm 0.03$. The exponents $g_P^{(1)}$, $g_P^{(2)}$, and d_P are given by Eqs. (2.24), (2.26), and (2.28), respectively. In the unscaled coordinates, $P(t, r, L)$ under constant pressure is

$$P(t, r, L) \sim \left(\frac{t}{r^{d_B+\tilde{\mu}}}\right)^{-g_P^{(1)}} F_P\left(\frac{t}{r^{d_B+\tilde{\mu}}}\right) G\left(\frac{t}{L^{d_P} r^{-d_P+d_B+\tilde{\mu}}}\right). \tag{2.50}$$

For the case of constant current, we have

$$P(t_C) \sim t_C^{-g_C^{(1)}} F_C(t_C) H_1\left(\frac{t_C}{\lambda^{d_C^{(1)}}}\right) H_2\left(\frac{t_C}{\lambda^{d_C^{(2)}}}\right). \tag{2.51}$$

The function $F_C(x)$ corresponds to a stretched exponential

$$F_C(x) \sim \exp(-cx^{-\theta}), \tag{2.52}$$

where again the constants c and θ are fitted by the data. By completing the necessary transformations on Fig. 2.2(b), we obtain $\theta = -1.49 \pm 0.01$. The functions H_1 and H_2 are given by

$$H_1(x) \sim \begin{cases} const. & x \ll 1 \\ x^{-g_C^{(2)}+g_C^{(1)}} & x \gg 1 \end{cases} \tag{2.53}$$

and

$$H_2(x) \sim \begin{cases} const. & x \ll 1 \\ x^{-g_C^{(3)}+g_C^{(3)}} & x \gg 1. \end{cases} \tag{2.54}$$

Once again, the exponents $g_C^{(1)}$, $g_C^{(2)}$, $g_C^{(3)}$, $d_C^{(1)}$, and $d_C^{(2)}$, are given by the Eqs. (2.33), (2.35), (2.38), (2.40), and (2.42), respectively. For the unscaled coordinates, we find

$$P(t,r,L) \sim \left(\frac{t}{r^{d_B}}\right)^{-g_C^{(1)}} F_C\left(\frac{t}{r^{d_B}}\right) H_1\left(\frac{t}{L^{d_C^{(1)}} r^{-d_C^{(1)}+d_B}}\right) H_2\left(\frac{t}{L^{d_C^{(2)}} r^{-d_C^{(2)}+d_B}}\right). \tag{2.55}$$

An additional constraint that Eq. (2.51) has to satisfy is that of the equal-time theorem (we treat the scaled coordinates example). The flow of tracers occurs only on the backbone of the percolation clusters, which has volume proportional to M_B, and the total tracer current Q is unity. Since we use all backbones that connect points A and B, without requiring that they percolate throughout the entire system $L \times L$, we expect that the average time $\langle t_C \rangle$ scales with λ exactly in the same way as $\langle M_B \rangle$ scales for a given λ.

The problem of the distribution of backbone masses M_B of a percolation cluster defined between two points A and B, separated by a distance r, for a given system of size $L \times L$, is treated in [57], and it is predicted that

$$\langle M_B \rangle \sim \frac{L^{d_B}}{\lambda^{\psi}} \qquad \psi = 0.37 \pm 0.02. \tag{2.56}$$

Therefore, applying the equal-time theorem

$$\langle t_C \rangle = \frac{\langle t \rangle}{r^{d_B}} \sim \frac{\langle M_B \rangle}{r^{d_B}} \sim \lambda^{d_B - \psi}. \tag{2.57}$$

Calculating $\langle t_C \rangle$ from Eq. (2.51), we find that it scales as a power of λ^{ξ}, where ξ depends on the exponents involved in Eq. (2.51). Noting that $g_C^{(2)}$ has a decreasing value which is λ dependent and that this regime extends to $\tau_C^{(2)} \sim \lambda^{d_\times}$, to satisfy Eq. (2.57), ξ must satisfy

$$\xi = d_B - \psi = (2 - g_C^{(2)}) d_\times, \tag{2.58}$$

which implies that $g_C^{(2)} \approx 1.55$, very close to the value of the exponent $g_C^{(1)}$. Therefore, we expect that

$$g_C^{(2)} \to g_C^{(1)} \qquad [\lambda \to \infty] \tag{2.59}$$

and the power-law regions III_C and IV_C become one region, with exponent $g_C^{(1)}$ extending from the maximum of $P(t_C)$ to the crossover time $\tau_C^{(2)}$.

Finally, regarding the validity of our results in true field-size porous media, we hypothesize that the form of the scaling *ansatz* presented still holds, even if the values of the exponents change. This issue must be resolved by additional studies.

2.8 Conclusions

We establish that the distributions of traveling times obey the general scaling relations $P(t, r, L) = (1/r^z) P(t/r^z, 1, \lambda)$, and the production curve satisfies $C(t, r, L) = C(t/r^z, 1, \lambda)$. For constant pressure conditions, $z = d_B + \tilde{\mu}$, and for constant current, $z = d_B$. This relates the scaling of the traveling time to the scaling of two basic cluster properties: backbone and conductivity.

Using the rescaled times $t_P \equiv t/r^{d_B + \tilde{\mu}}$ and $t_C \equiv t/r^{d_B}$, we have determined the dependence of $P(t_P) = P(t_P, 1, \lambda)$ and $P(t_C) = P(t_C, 1, \lambda)$ on the geometric parameter λ and have observed several power law regions. We obtain the exponents for the power law regions and crossover times of $P(t_P)$ and $P(t_C)$ by convolution of the functions $P(t_P|R)$ and $\Phi(R)$, expressed as functions of the exponents g_R, d_R, $d_\times$, $\gamma^{(1)}$, and $\gamma^{(2)}$. The crossover times themselves scale as powers of the ratio λ. We propose relations between d_R and $d_\times$ and the fundamental percolation exponents d_B and $\tilde{\mu}$. Using arguments based on multifractality, we also propose the relation $\gamma^{(2)} = 2 + a/\log_{10} L$. The exponent $\gamma^{(1)}$ is not yet explained (see Table 2.2). The full scaling forms of $P(t_P)$ and $P(t_C)$ are expressed in two scaling *ansatz* (Eqs. (2.47) and (2.51)) that contain all their observed regions and crossover times.

For the longest times, the crossover occurs for the $p = 1$ case at a time that scales as λ^{d_l}, with $d_l = 3$, which can be interpreted as $d_B + \tilde{\mu}$ under homogeneous conditions. For the $p = p_c$ case, the crossover to the long time region scales as $\lambda^{d_\times}$, regardless of the pumping conditions (constant current or constant pressure). We hypothesize that $d_\times$ and $d_B + \tilde{\mu}$ are the same exponent and propose that the transition to the long time regime occurs similarly at different values of the occupation probability p.

2.9 Analytical solution for the homogeneous case

The equations for the stationary ideal flow [52] are $\nabla^2 P = 0$ and $\vec{v} = \vec{\nabla} P$, where P is the pressure, $\vec{v}$ the velocity and ∇^2 is the Laplace operator. In two dimensions, the solution is given by an arbitrary analytical function $f(z)$ of complex variable $z = x + iy$, and $P(x, y) = Ref(z)$, $v_x = Ref'(z)$ and $v_y = -Imf'(z)$. The equation of a streamline is given by $\phi = Imf(z)$, where ϕ is a parameter. The flow between two wells A and B, located at points $(\pm r/2, 0)$ in the circular reservoir $x^2 + y^2 \leq L^2/4$, is given by

$$f(z) = \ln\left(z + \frac{r}{2}\right) - \ln\left(z - \frac{r}{2}\right) + \ln\left(z + \frac{L^2}{2r}\right) - \ln\left(z - \frac{L^2}{2r}\right). \qquad (2.60)$$

The circular boundary of the reservoir satisfies the equation $\phi = \pi$. The fastest streamline connecting A and B corresponds to $\phi = 0$ and an arbitrary streamline forms angles ϕ and $(\pi - \phi)$ with the x-axis at points A and B. The traveling time along a streamline can be found as a contour integral

$$t = \int_A^B \frac{dz}{\overline{f'(z)}} = \int_A^B \frac{dx}{v_x} = \int_A^B \frac{dy}{v_y}, \tag{2.61}$$

where $\overline{f'(z)}$ is the complex conjugate of $f'(z)$. The traveling time $t(\phi)$ can also be found by differentiation of the area $S(\phi)$ between two streamlines corresponding to different values of ϕ

$$t(\phi) = \frac{dS(\phi)}{d\phi}, \tag{2.62}$$

which is another manifestation of the equal-time theorem. The concentration of oil arriving at the well B at time t i.e., the production curve $C(t,r)$, is given by the inverse of function $\phi(t)$

$$C(t,r) = \frac{\pi - \phi(t)}{\pi}. \tag{2.63}$$

In the unbounded case, $L \to \infty$, the streamlines are circles, and $t(\phi)$ is given by an elementary formula

$$t = \frac{r^2}{2\sin^2\phi}\left(1 - \frac{\phi\cos\phi}{\sin\phi}\right). \tag{2.64}$$

Thus t has dimensionality of area and therefore in the following, we use the scaled time $t' = t/r^2$. Accordingly, $C(t,r)$ has the scaling property

$$C(t,r) = C(t' = t/r^2, 1). \tag{2.65}$$

In the interest of briefness, we use $C(t') \equiv C(t',1)$. For small $\phi \to 0$, t' is given by the expansion

$$t' = \frac{1}{6} + \frac{1}{15}\phi^2 + O(\phi^4). \tag{2.66}$$

For large $\phi \to \pi$, $t' \to \infty$ and

$$t' = \frac{\pi}{2(\pi - \phi)^3}[1 + O((\pi - \phi)^2)]. \tag{2.67}$$

The breakthrough time t'_{br} corresponds to the fastest streamline $\phi = 0$ and thus is given by

$$t'_{\mathrm{br}} = \lim_{\phi \to 0} t'(\phi) = \frac{1}{6}. \tag{2.68}$$

Immediately after breakthrough, the concentration of oil drops as

$$C(t') = 1 - K\sqrt{t' - t'_{\rm br}} + O((t' - t'_{\rm br})^{3/2}), \tag{2.69}$$

where $K = \frac{\sqrt{15}}{\pi}$. When $t' \to \infty$, the concentration decays as a power law

$$C(t') = \left(\frac{1}{2\pi^2 t'}\right)^{\frac{1}{3}} + O\left(\frac{1}{t'}\right). \tag{2.70}$$

The crossover time from the initial fast decay to the slow power law decay is approximately equal to the time $t'_{1/2}$, defined as the time when the concentration drops by a factor of two, or $t'_{1/2} = t'(\pi/2) = 1/2$.

In the bounded case, the production curve for scaled time depends only on the ratio $\lambda \equiv L/r$, and similarly to the result of Eq.(2.65), we find that

$$C(t, r, L) = C(t' = t/r^2, 1, \lambda). \tag{2.71}$$

The production curve $C(t', \lambda) \equiv C(t' = t/r^2, 1, \lambda)$ can be expressed via elliptical functions. Integrating Eq. (2.61) along the fastest streamline gives

$$t'_{\rm br} = \frac{1 + \lambda^6 + (1 - \lambda^2)^3}{12(1 + \lambda^2)} + \frac{\lambda(1 - \lambda^2)^2}{8(1 + \lambda^2)} \ln\left(\frac{\lambda - 1}{\lambda + 1}\right), \tag{2.72}$$

which in the limit $\lambda \to \infty$ yields

$$t'_{\rm br} = \frac{1}{6} - \frac{2}{15}\lambda^{-2} + o(\lambda^{-2}). \tag{2.73}$$

The constant K in the initial fast decay can be obtained by expanding the equations of short streamlines in powers of ϕ, resulting in lengthy elementary functions of λ. Expanding the latter in powers of λ^{-1} yields

$$K = \frac{\sqrt{15}}{\pi}\left[1 + \frac{10}{7}\lambda^{-2} + o(\lambda^{-2})\right]. \tag{2.74}$$

The half time is given by integration along the $\phi = \pi/2$ streamline

$$\begin{aligned} t'_{1/2} &= \frac{1}{4}\left[1 + \lambda^2 - \frac{(1 + \lambda^2)^3}{4\lambda} \arcsin\left[\frac{4}{(1 + \lambda^2)\sqrt{\lambda^2 + 6 + \lambda^{-2}}}\right]\right] \\ &= \frac{1}{2} + O(\lambda^{-2}). \end{aligned} \tag{2.75}$$

Finally, as $t' \to \infty$ and $\phi \to \pi$, the entire reservoir is swept out except in the vicinity of the two stagnation points $(\pm L/2, 0)$, where the velocity is equal to zero. Integrating Eq. (2.61) along the reservoir boundary and the segments connecting the wells and stagnation points, with the exception of a small vicinity of the stagnation point of order $\sqrt{\pi - \phi}$, gives

$$t' = t'_o - t'_\ell \ln(\pi - \phi) + o(1), \tag{2.76}$$

where t'_o and t'_ℓ are functions of λ,

$$t'_\ell = \frac{1}{8} \frac{\lambda(\lambda^2 - 1)^2}{(\lambda^2 + 1)} = \frac{\lambda^3}{8} + O(\lambda), \tag{2.77}$$

and

$$t'_o = t'_\ell \left[\frac{2(2 - 3\lambda - 3\lambda^2 + 10\lambda^3 + 3\lambda^4 - 3\lambda^5)}{3\lambda(\lambda^2 - 1)^2} + \ln \frac{16\lambda(\lambda^2 + 1)}{(\lambda^2 - 1)(\lambda + 1)^2} \right]. \tag{2.78}$$

This yields the exponential decay of $C(t')$ at $t' \to \infty$

$$C(t') = \frac{1}{\pi} \exp\left[-\frac{(t' - t'_o)}{t'_\ell} \right] [1 + o(1)], \tag{2.79}$$

where t'_ℓ plays the role of the characteristic time. If $t'_\ell > t'_{1/2}$ ($\lambda \gg 1$), an intermediate power law decay is present between $t'_{1/2}$ and t'_ℓ, with the scaling form of Eq. (2.70). In this case, t'_ℓ also plays the role of the crossover time from the power law to the exponential decay.

Constant Current		
Region	Theory	Simulation
III_C	$g_C^{(1)} = \min\left\{(d_R + g_R - 2)/(d_R - 1), \gamma^{(1)}\right\}$ $= \min\{1.70 \pm 0.13, 1.74 \pm 0.15\}$	1.56 ± 0.01
IV_C $(\lambda \approx 32)$	$g_C^{(2)} = \min\{(\gamma^{(1)} - 1)d_R - g_R + 2, \gamma^{(1)}\}$ $= \min\{1.80 \pm 0.40, 1.74 \pm 0.15\}$	1.75 ± 0.01
IV_C $(\lambda \to \infty)$	$g_C^{(2)} \to g_C^{(1)} \approx 1.56 \pm 0.01$	N/A
V_C	$g_C^{(3)} = \gamma^{(2)} = 2 + a/\log_{10} L$	2.45 ± 0.04 (Avg.)
crossover $\tau_C^{(1)}$	$d_C^{(1)} = d_\times (d_R - 1)/d_R = 1.73 \pm 0.07$	1.74 ± 0.05
crossover $\tau_C^{(2)}$	$d_C^{(2)} = d_\times = 2.84 \pm 0.10$	2.90 ± 0.09
Constant Pressure		
Region	Theory	Simulation
III_P	$g_P^{(1)} = (d_R + g_R - 1)/d_R = 1.43 \pm 0.08$	1.41 ± 0.01
IV_P	$g_P^{(2)} = \gamma^{(2)} = 2 + a/\log_{10} L$	2.43 ± 0.06 (Avg.)
crossover τ_P	$d_P = d_\times = 2.84 \pm 0.10$	2.78 ± 0.15

Table 2.1: Theoretical exponents and exponents obtained by simulation for the all the regions and crossovers for the functions $P(t_C)$ and $P(t_P)$. The exponents $\gamma^{(1)}$, $\gamma^{(2)}$, d_R, and $d^\times$ are defined in Sec. 2.7 and their numerical values along with their proposed theoretical values can be found in Table 2.2. The value of the exponent $\gamma^{(2)}$ was obtained as the average (Avg.) over three simulations, having $L = 258, 514, 1026$.

Exponent	Theory	Simulation
$\gamma^{(1)}$	N/A	1.74 ± 0.15
$\gamma^{(2)}$	$2 + a/\log_{10} L$	2.41 ± 0.04 (Avg.)
d_R	$d_B/\tilde{\mu} + 1 = 2.672 \pm 0.002$	2.57 ± 0.02
$d_\times$	$d_B + \tilde{\mu} = 2.6258 \pm 0.0011$	2.84 ± 0.10
g_R	See [13]	2.10 ± 0.20

Table 2.2: Exponents of the functions $P(t_P|R)$ and $\Phi(R)$ determined through simulations, and also their proposed theoretical values. The symbol N/A represents not available. The value of the exponent $\gamma^{(2)}$ was obtained as the average (Avg.) over three simulations, having $L = 258, 514, 1026$.

Chapter 3

Possible Connection between the Optimal Path and Flow in Percolation Clusters

3.1 Overview

We study the behavior of the optimal path between two sites separated by a distance r on a d-dimensional lattice of linear size L with weight assigned to each site. We focus on the strong disorder limit, i.e., when the weight of a single site dominates the sum of the weights along each path. We calculate the probability distribution $P(\ell_{\rm opt}|r, L)$ of the optimal path length $\ell_{\rm opt}$, and find for $r \ll L$ a power law decay with $\ell_{\rm opt}$, characterized by exponent $g_{\rm opt}$. We determine the scaling form of $P(\ell_{\rm opt}|r, L)$ in two- and three-dimensional lattices. To test the conjecture that the optimal paths in strong disorder and flow in percolation clusters belong to the same universality class, we study the tracer path length $\ell_{\rm tr}$ of tracers inside percolation through their probability distribution $P(\ell_{\rm tr}|r, L)$. We find that, because the optimal path is not constrained to belong to a percolation cluster, the two problems are different. However, by constraining the optimal paths to remain inside the percolation clusters in analogy to tracers in percolation, the two problems exhibit similar scaling properties.

3.2 Introduction

It is often assumed that transport properties on percolation clusters can be directly related to some geometric property of the cluster, but despite considerable effort [58] such a geometric property relation has not been found [59]. Flow in porous media can be modeled by flow in percolation systems [60], and the most probable traveling length $\ell_{\rm tr}$ of a convective tracer on a percolation cluster scales with the distance r between the injection and extraction sites A and B [12] as

$$\ell_{\rm tr} \sim r^{d_{\rm tr}} \qquad [d_{\rm tr} = 1.21 \pm 0.02 \ \text{ for } \ d = 2]. \tag{3.1}$$

For $d = 2$, the exponent $d_{\rm tr} \approx d_{\rm opt}$ where $d_{\rm opt}$ is the exponent for the optimal path length in the strong disorder limit [31, 61].

In this study, we propose that transport in percolation can be directly related to the optimal path in strong disorder, and we support our proposal with extensive numerical simulations for d-dimensional lattices with $d = 2$ and 3.

The optimal path is defined as follows: for a d-dimensional lattice to each site (or bond) i, we associate a weight $\epsilon_i = e^{ax_i}$, with $x_i \in [0, 1)$. This is equivalent to choosing ϵ_i from the distribution

$$W(\epsilon) = \frac{1}{a\epsilon} \qquad \epsilon \in [1, \exp a]. \tag{3.2}$$

The energy of any path of length ℓ on the lattice is given by the sum

$$E \equiv \sum_{j}^{\ell} \epsilon_j, \tag{3.3}$$

where j is an index running over the sites of the path. The limit $a \to \infty$ is known as the strong disorder limit. The optimal path of length $\ell_{\rm opt}$ is the path for which E

is minimal with respect to all other paths. The optimal path length scales with r as [31]

$$\ell_{\rm opt} \sim r^{d_{\rm opt}} \qquad [d_{\rm opt} = 1.22 \pm 0.01]. \tag{3.4}$$

We address the question: can flow on percolation clusters in strong disorder, a dynamical process, be connected to the optimal path in strong disorder, a static property, as suggested by the similarity of Eqs. (3.1) and (3.4)? To this end, we study the probability density function (pdf) $P(\ell_{\rm opt}|r,L)$ for the optimal path to have a length $\ell_{\rm opt}$, given a system size L, and an Euclidean distance r between the starting and ending sites A and B of the path. We will compare this pdf with $P(\ell_{\rm tr}|r,L)$, the pdf that convective tracer paths have a length $\ell_{\rm tr}$ in a percolation system of size L at criticality, where the starting and ending sites are at a distance r.

Other relations between percolation and strong disorder optimal path have been reported. For a lattice with disorder given by Eq. (3.2) in the strong disorder limit, the most probable largest weight of the sites used by the optimal path is e^{ap_c}, where p_c is the percolation threshold [61]. Also, Wu et al. [62] recently determined through the study of tracer flow on a lattice with disorder, that the strong disorder limit has a length scale that scales as a^{ν}, where ν is the connectedness exponent of percolation [60], and hence a system is in the strong disorder limit only when $a^{\nu} > L$. In this paper, we study the ultrametric limit $a \to \infty$.

In Sec. 3.3 we present results for the distribution $P(\ell_{\rm opt}|r,L)$. In Sec. 3.4, results for $P(\ell_{\rm tr}|r,L)$ are presented and compared with $P(\ell_{\rm opt}|r,L)$. We then discuss the results in Sec. 3.5.

3.3 Optimal Path Distribution

To study $P(\ell_{\rm opt}|r,L)$ we use the "bombing algorithm" proposed in Ref. [31]. The optimal path length $\ell_{\rm opt}$ between sites A and B is found by eliminating sites of the lattice in decreasing order of weight, but leaving those sites necessary to keep A and

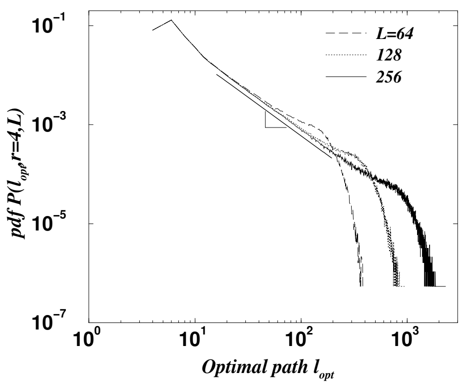

Figure 3.1: Distribution $P(\ell_{\rm opt}|r,L)$ for $r=4$ and system sizes $L=64,128$ and 256. As L increases, the power law region with exponent $g_{\rm opt}$ becomes better defined, and the upper cutoff increases.

B connected. When all sites that do not disconnect A and B are eliminated, only the sites of the optimal path remain [63, 64, 65].

In Figs. 3.1, 3.2 and 3.3 we present $P(\ell_{\rm opt}|r,L)$ for $r \ll L$ for a square lattice of sites. Four distinct features appear:

- The most probable optimal path length $\ell^*_{\rm opt}$ scales with r as

$$\ell^*_{\rm opt} \sim r^{d_{\rm opt}}. \tag{3.5}$$

  The values of $d_{\rm opt}$ have been reported for several lattice dimensions d, and also have been shown to be universal [66]. Here, we rescale $P(\ell_{\rm opt}|r,L)$ with the exponent $d_{\rm opt}$, calculated elsewhere for the average optimal path length $\bar{\ell}_{\rm opt}$, but, as Figs. 3.1 and 3.2 show, $d_{\rm opt}$ also produces the correct scaling for $\ell^*_{\rm opt}$. Our results for $d_{\rm opt}$ are reported in Table 3.1 for $d=2$ and 3.

- A lower cutoff [Fig. 3.2] which, in analogy with the distribution of minimal paths in percolation [67, 68, 13], is expected to be a stretched exponential function f_1 of the form

$$f_1(x) = \exp(-\alpha x^{-\phi_{\rm opt}}) \qquad \left[x \equiv \frac{\ell_{\rm opt}}{r^{d_{\rm opt}}}\right], \tag{3.6}$$

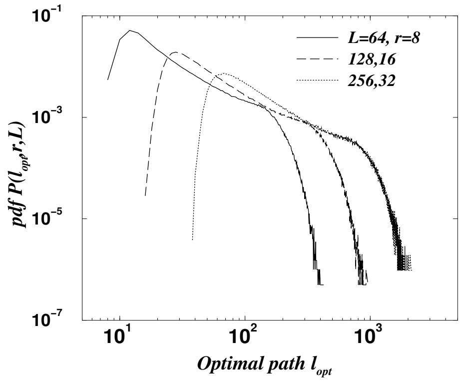

Figure 3.2: (b) Probability distribution $P(\ell_{\rm opt}|r,L)$ for $(r=8, L=64)$ (solid line), $(r=16, L=128)$ (dashed line), and $(r=32, L=256)$ (dotted line) for two-dimensional systems. The ratio between L and r is kept fixed for these curves.

where α is a lattice-dependent constant, and $\phi_{\rm opt}$ is a universal exponent satisfying [66, 67]

$$\phi_{\rm opt} = \frac{1}{d_{\rm opt}-1}. \tag{3.7}$$

- An upper cutoff due to the effect of the finite lattice size L. A stretched exponential behavior is also expected to describe this region [64, 68, 13], through a function f_2 of the form

$$f_2(y) = \exp(-\beta y^{\psi_{\rm opt}}) \qquad \left[y \equiv \frac{\ell_{\rm opt}}{L^{d_{\rm opt}}} \right], \tag{3.8}$$

where β is a lattice-dependent constant, and $\psi_{\rm opt}$ has universal properties [64, 68, 13].

- A power-law region described by

$$P(\ell_{\rm opt}) \sim \ell_{\rm opt}^{-g_{\rm opt}} \qquad [r^{d_{\rm opt}} < \ell_{\rm opt} \leq L^{d_{\rm opt}}]. \tag{3.9}$$

The above considerations lead us to postulate for $P(\ell_{\rm opt}|r,L)$ a full scaling *Ansatz* [66, 67, 68, 13]

$$P(\ell_{\rm opt}|r,L) \sim \frac{1}{r^{d_{\rm opt}}} \left(\frac{\ell_{\rm opt}}{r^{d_{\rm opt}}}\right)^{-g_{\rm opt}} f_1\left(\frac{\ell_{\rm opt}}{r^{d_{\rm opt}}}\right) f_2\left(\frac{\ell_{\rm opt}}{L^{d_{\rm opt}}}\right), \tag{3.10}$$

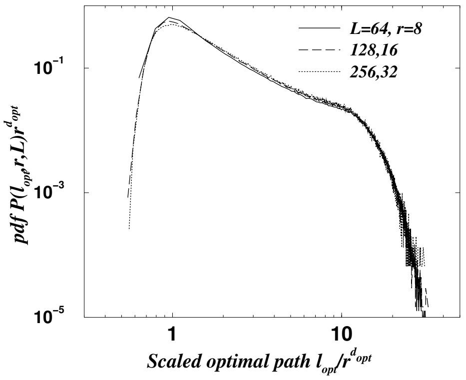

Figure 3.3: (c) Scaled distribution $r^{d_{\rm opt}}P(\ell_{\rm opt}|r,L)$ vs. scaled optimal path length $\ell_{\rm opt}/r^{d_{\rm opt}}$ for the curves in Fig. 3.2. The collapse has been achieved using the exponent $d_{\rm opt}$ reported for $\bar{\ell}_{\rm opt}$, which is also valid for the most probable length $\ell^*_{\rm opt}$ as evidenced in the plot.

where the prefactor $1/r^{d_{\rm opt}}$ is necessary for normalization. We have tested this *Ansatz* for $d = 2$, 3 and found it to be consistent with our earlier simulations [66].

An interesting feature of $P(\ell_{\rm opt}|r,L)$ is that, as d increases, $g_{\rm opt}$ decreases. In other words, the longer optimal paths at larger dimensions have a larger probability (see Table 3.1). Additionally, since $g_{\rm opt} < 2$ for all d, $\bar{\ell}_{\rm opt}$ and all higher moments diverge as $L \to \infty$.

To calculate the exponents $\phi_{\rm opt}$ and $\psi_{\rm opt}$ of Eqs. (3.6) and (3.8), we introduce the function

$$\Pi\left(\frac{\ell_{\rm opt}}{r^{d_{\rm opt}}}, \lambda, A\right) \equiv \ln\left[\frac{A}{P(\ell_{\rm opt}|r,L)r^{d_{\rm opt}}\left(\frac{\ell_{\rm opt}}{r^{d_{\rm opt}}}\right)^{g_{\rm opt}}}\right] \tag{3.11}$$

which, upon using Eqs. (3.6), (3.8) and (3.10) yields

$$\begin{aligned}\Pi\left(\frac{\ell_{\rm opt}}{r^{d_{\rm opt}}}, \lambda, A\right) &\sim \ln\left[\frac{A}{f_1\left(\frac{\ell_{\rm opt}}{r^{d_{\rm opt}}}\right) f_2\left(\frac{\ell_{\rm opt}}{r^{d_{\rm opt}}}\lambda^{-d_{\rm opt}}\right)}\right] \\ &\sim \ln A + \alpha\left(\frac{\ell_{\rm opt}}{r^{d_{\rm opt}}}\right)^{-\phi_{\rm opt}} + \beta\left(\frac{\ell_{\rm opt}}{r^{d_{\rm opt}}}\lambda^{-d_{\rm opt}}\right)^{\psi_{\rm opt}}.\end{aligned} \tag{3.12}$$

We have made use of $\lambda \equiv L/r$ in the argument of the function f_2 so that $f_2(\ell_{\rm opt}/L^{d_{\rm opt}}) =$

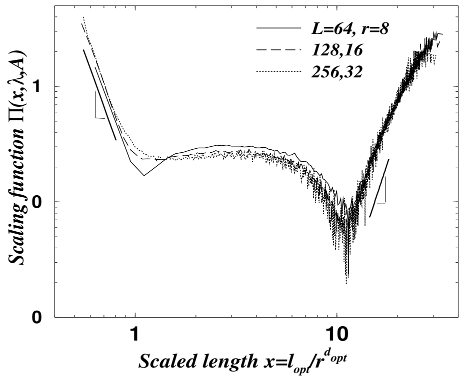

Figure 3.4: The scaling function $\Pi(x, \lambda, A)$ for $A = 0.1$ vs. the scaled optimal path length $x \equiv \ell_{\rm opt}/r^{d_{\rm opt}}$ for system sizes $(r = 8, L = 64)$, $(r = 16, L = 128)$, and $(r = 32, L = 256)$. The two straight lines serve as guides to the eye for the data that determine the exponents $\phi_{\rm opt}$ and $\psi_{\rm opt}$.

$f_2(\lambda^{-d_{\rm opt}}\ell_{\rm opt}/r^{d_{\rm opt}})$. The constant A is an auxiliary parameter chosen to make the minimum value of Π slightly larger than unity. Defining $x \equiv \ell_{\rm opt}/r^{d_{\rm opt}}$, we show in Fig. 3.4 $\Pi(x, \lambda, A)$ for $d = 2$ and the fit lines for the exponents of both f_1 and f_2, which are reported in Table 3.1. The values of $\phi_{\rm opt}$ we calculate are close to the values predicted by Eq. (3.7) for $d = 2$, 3.

3.4 Comparison between Flow in Percolation and the Optimal path

The question of whether the optimal path $\ell_{\rm opt}$ is related to the flow of tracers on a percolation cluster has remained unsolved. This question was raised [12] due to a puzzling coincidence of the scaling exponent $d_{\rm tr}$ of the typical tracer length which, for $d = 2$, is within error of $d_{\rm opt}$. It was then proposed that the traveling lengths $\ell_{\rm tr}$ of tracers driven by convection on a percolation cluster satisfy the same scaling laws as those for $\ell_{\rm opt}$. Here, we address this question by analyzing the detailed conditions under which optimization and flow in percolation occur. Our analysis (see Sec. 3.5) explains the differences we observe, and also the "right way" in which the two problems become equivalent.

Since simulations for flow on percolation clusters are performed, we describe the two-dimensional case of the algorithm. We follow closely the description made in Ref. [30]. We represent the reservoir as a two-dimensional site percolation cluster, and choose sites at $(-r/2, 0)$ and $(r/2, 0)$, denoted by A and B, respectively, to be the injection and extraction well positions. Points A and B are separated by a geometric distance r, and the system box has corners at $(\pm L/2, \pm L/2)$. We construct percolation clusters at p_c using the Leath algorithm [69].

To model tracer motion we use the analogy with electrical circuits, where for each bond, the pressure drop corresponds to the voltage difference, and the flow corresponds to the electrical current on the bond. A pressure difference between sites A and B drives the tracer. For each realization, 10^4 tracers are introduced at site A, and then collected at site B. The set of all sites through which there is a non-zero current defines the cluster backbone of M_B sites.

The "pressure" difference across bonds is equivalent to a "voltage" difference, so by solving Kirchhoff's equations on the backbone, we obtain the potential (pressure) drops ΔV over all bonds for a given realization. For site i having s_i outgoing bonds, the tracer selects a bond with a probability

$$w_{ij} \equiv \frac{\Delta V_{ij}}{\sum_j \Delta V_{ij}} \quad [j = 1, \ldots, s_i;\ i = 1, \ldots, M_B]. \tag{3.13}$$

For incoming bonds, $w_{ij} = 0$. The total traveling length of a tracer is the number of bonds of the path connecting A and B, chosen by this tracer. Since the particles do not interact with one another, it is equivalent to launching one particle at a time into the cluster. This procedure is known as *particle launching algorithm* [52, 53]. We determine the probability distribution of the tracer traveling lengths $P(\ell_{\rm tr}|r, L)$ by counting the number of particles that travel from site A to site B along a path of

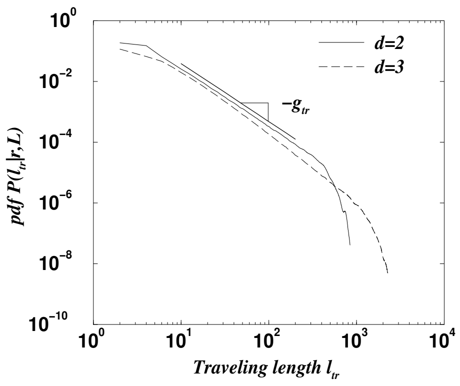

Figure 3.5: Probability distribution $P(\ell_{\mathrm{tr}}|r, L)$ for $r = 2$ and $L = 128$ in $d = 2$ and $d = 3$. In a similar fashion as for $P(\ell_{\mathrm{opt}}|r, L)$ we see a power law region that we characterize by exponent g_{tr}. Another feature of this plot is the increasing steepness of $P(\ell_{\mathrm{tr}}|r, L)$ as d increases (implying g_{tr} increases with d), a feature for which $P(\ell_{\mathrm{opt}}|r, L)$ has the opposite behavior, as g_{opt} decreases with d.

length ℓ_{tr}, over all the particles and all realizations of the percolation cluster.

The form of $P(\ell_{\mathrm{tr}}|r, L)$ for the two-dimensional case was suggested in [12]. Here, we extend these results to $d = 3$ (Fig. 3.5). Once again, the power law and stretched exponential behaviors are present. The scaling of the most probable tracer path length is given by $\ell_{\mathrm{tr}}^* \sim r^{d_{\mathrm{tr}}}$. These results yield

$$P(\ell_{\mathrm{tr}}|r, L) \sim \frac{1}{r^{d_{\mathrm{tr}}}} \left(\frac{\ell_{\mathrm{tr}}}{r^{d_{\mathrm{tr}}}}\right)^{-g_{\mathrm{tr}}} h_1\left(\frac{\ell_{\mathrm{tr}}}{r^{d_{\mathrm{tr}}}}\right) h_2\left(\frac{\ell_{\mathrm{tr}}}{L^{d_{\mathrm{tr}}}}\right), \tag{3.14}$$

where functions h_1 and h_2 have the forms

$$h_1(z) = \exp(-\mu z^{-\phi_{\mathrm{tr}}}) \qquad \left[z \equiv \frac{\ell_{\mathrm{tr}}}{r^{d_{\mathrm{tr}}}}\right], \tag{3.15}$$

and

$$h_2(u) = \exp(-\rho u^{\psi_{\mathrm{tr}}}) \qquad \left[u \equiv \frac{\ell_{\mathrm{tr}}}{L^{d_{\mathrm{tr}}}}\right]. \tag{3.16}$$

Arguments similar to those leading to Eq. (3.12) indicate how to determine the exponents ϕ_{tr} and ψ_{tr}, reported in Table 3.1.

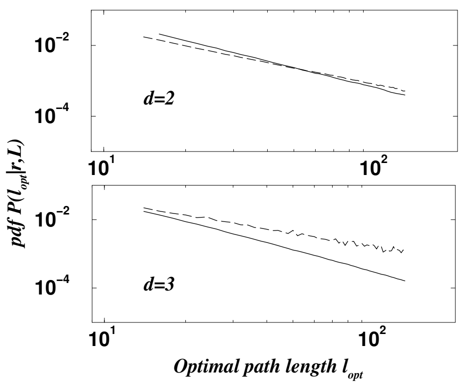

Figure 3.6: The power law tails of $P(\ell_{\rm tr}|r,L)$ (solid) and $P(\ell_{\rm opt}|r,L)$ (dashed) in $d=2$ and 3. The upper pair is for $d=2$ with $L=256$ and $r=4$. The lower pair is for $d=3$ with $L=128$ and $r=2$.

The power law region is characterized by the exponent $g_{\rm tr}$, which is different from $g_{\rm opt}$ (see Table 3.1). We present in Fig. 3.6 curves for the power law regime for both $P(\ell_{\rm tr}|r,L)$ and $P(\ell_{\rm opt}|r,L)$ in $d=2$ and 3. In Table 3.1 we see the difference in the slope of the power law decay between $P(\ell_{\rm tr}|r,L)$ and $P(\ell_{\rm opt}|r,L)$. Moreover, as d increases, $g_{\rm opt}$ decreases and $g_{\rm tr}$ increases, indicating the differing behaviors for the two problems. In the next section, we explain the origin of the differences, how these differences can be removed, and under which conditions the two problems coincide.

3.5 Discussion

The numerical results presented above show the difference in the values of the scaling exponents $g_{\rm opt}$ and $g_{\rm tr}$ of the distributions. To understand these differences, we now elaborate on the characteristics of the optimal path problem in comparison to those of tracer paths in percolation.

In Fig. 3.7(a) we represent the optimal path in strong disorder, where the dark areas represent regions with site weights $\epsilon_i = e^{ax_i}$ with $x_i \le p_c$, and the white areas

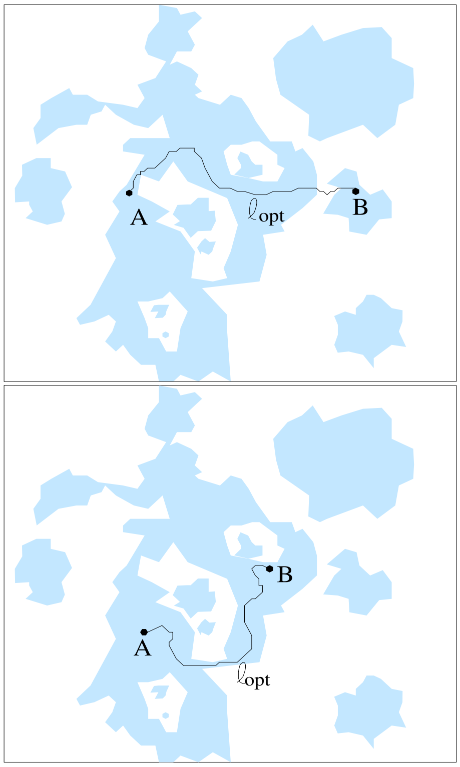

Figure 3.7: (a) Schematic of occupied sites for p below the percolation threshold p_c, and the optimal path in strong disorder. The darker regions represent sites that are still present when p_c is reached. We see in this case that ℓ_{opt} must cross the region above p_c (i.e., leave the cluster) to connect A and B. (b) If sites A and B are chosen within the a cluster below p_c, the optimal path does not leave the cluster because that would increase the cost.

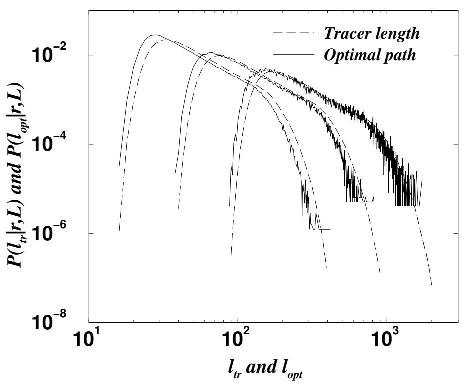

Figure 3.8: Comparison of $P(\ell_{opt}|r, L)$ inside percolation with $P(\ell_{\rm tr}|r, L)$ for $(r = 16, L = 64)$, $(r = 32, L = 128)$ and $(r = 64, L = 256)$. The solid lines represent the optimal path distribution, and the long dashed lines the tracer length distributions. The values of r and L have a fixed ratio equal to $L/r = 4$. The similarity between distributions is clear, supporting our hypothesis. The small separation along the horizontal axis between $P(\ell_{opt}|r, L)$ and $P(\ell_{\rm tr}|r, L)$ (consistent for the three pairs of curves) is due to non-universal details of the two models.

regions with site weigths $\epsilon = e^{ax_i}$ with $x_i > p_c$. Typically, the arbitrary choice of A and B may lead to a path connecting them that requires visiting regions with site weights $\epsilon > e^{ap_c}$. In contrast, the tracers inside percolation clusters must, by definition, travel on the *same* percolation cluster (spanning or otherwise), because the flow takes place only if there is a percolating path between A and B. Therefore, this difference between the flow and optimal path problems presents a possible explanation for the differences between $P(\ell_{\rm opt}|r, L)$ and $P(\ell_{\rm tr}|r, L)$. Optimal paths tend to be longer because they are able to visit more sites of the lattice and are therefore of longer length, whereas tracers in percolation flow are confined to a given cluster, and their traveling lengths are much more limited. These features intuitively explain why $g_{\rm tr}$ is larger than $g_{\rm opt}$.

The above considerations lead to the following hypothesis: if the optimal path search is constrained to pairs of sites within regions of the lattice that are part of the same cluster [Fig. 3.7(b)], then the scaling of $P(\ell_{\rm opt}|r,L)$ and $P(\ell_{\rm tr}|r,L)$ would coincide. To test this, we present $P(\ell_{\rm opt}|r,L)$ and $P(\ell_{\rm tr}|r,L)$ in Fig. 3.8, where the optimal paths satisfy the condition that their highest weight is at or below percolation. This condition forces the optimal paths to be inside percolation clusters. Indeed, for this case (Fig. 3.8), the two quantities exhibit very similar behavior, supporting our hypothesis. The exponent $g_{\rm opt}$ inside percolation now becomes very close to $g_{\rm tr}$. On the other hand, d_{opt} does not change, confirming the equivalence of the two problems. We also have similar results for three-dimensional lattices.

In summary, we have shown that $P(\ell_{\rm opt}|r,L)$ has a power law tail with an exponent $g_{\rm opt}$ which decays as d grows and is different from the power law tail of $P(\ell_{\rm tr}|r,L)$. This difference seems to be related to the fact that the optimal path crosses percolation clusters and thus tends to have longer lengths compared with tracers which are always inside percolation clusters. When $\ell_{\rm opt}$ is measured only inside percolation clusters, our results suggest $P(\ell_{\rm opt}|r,L)$ and $P(\ell_{\rm tr}|r,L)$ are equivalent and the two problems possibly belong to the same universality class.

Table 3.1: Exponents characterizing $P(\ell_{\rm opt}|r,L)$ and $P(\ell_{\rm tr}|r,L)$, which are defined in the text. The value of $g_{\rm opt}$ is determined from $P(\ell_{\rm opt}|r=4,L=256)$ in Fig. 3.1, for which the power law region is the longest. The values of $\phi_{\rm opt}$ and $\psi_{\rm opt}$ are from Fig. 2.

Optimal Path in Strong Disorder (“Static”)					
d	$d_{\rm opt}$	$g_{\rm opt}$	$\phi_{\rm opt}$	$\phi_{\rm opt}=\frac{1}{d_{\rm opt}-1}$	$\psi_{\rm opt}$
2	1.22 ± 0.01[31]	1.55 ± 0.05	4.8 ± 0.5	4.55 ± 0.21	5.3 ± 0.3
3	1.42 ± 0.02[70]	1.37 ± 0.05	2.1 ± 0.1	2.3 ± 0.1	4.3 ± 0.3
Optimal Path in Strong Disorder in Percolation (“Modified Static”)					
2	1.21 ± 0.02	1.82 ± 0.05	4.9 ± 0.4	4.76 ± 0.45	2.3 ± 0.4
3	1.40 ± 0.03	2.2 ± 0.1	2.0 ± 0.1	2.5 ± 0.2	3.6 ± 0.2
Tracer Path (“Dynamic”)					
d	$d_{\rm tr}$	$g_{\rm tr}$	$\phi_{\rm tr}$	$\phi_{\rm tr}=\frac{1}{d_{\rm tr}-1}$	$\psi_{\rm tr}$
2	1.21 ± 0.02[12]	1.82 ± 0.05	4.7 ± 0.4	4.76 ± 0.45	2.7 ± 0.2
3	1.37 ± 0.05	2.23 ± 0.09	1.81 ± 0.02	2.7 ± 0.4	3.46 ± 0.04

Part III

Complex Networks

Chapter 4

Anomalous Transport in Complex Networks

4.1 Overview

To study transport properties of complex networks, we analyze the equivalent conductance G between two arbitrarily chosen nodes of random scale-free networks with degree distribution $P(k) \sim k^{-\lambda}$ in which each link has the same unit resistance. We predict a broad range of values of G, with a power-law tail distribution $\Phi_{\rm SF}(G) \sim G^{-g_G}$, where $g_G = 2\lambda - 1$, and confirm our predictions by simulations. The power-law tail in $\Phi_{\rm SF}(G)$ leads to large values of G, thereby significantly improving the transport in scale-free networks, compared to Erdős-Rényi networks where the tail of the conductivity distribution decays exponentially. Based on a simple physical "transport backbone" picture we show that the conductances of scale-free and Erdős-Rényi networks are well approximated by $ck_Ak_B/(k_A + k_B)$ for any pair of nodes A and B with degrees k_A and k_B. Thus, a single parameter c characterizes transport on complex networks.

Recent research on the topic of complex networks is leading to a better understanding of many real world social, technological, and natural systems ranging from the World Wide Web and the Internet to cellular networks and sexual-partner networks [32]. One type of network topology that appears in many real world systems is the scale-free network [71], characterized by a scale-free degree distribution:

$$P(k) \sim k^{-\lambda}, \qquad k_{\min} \leq k \leq k_{\max}, \tag{4.1}$$

where k, the degree, is the number of links attached to a node. The distribution has two cutoff values for k: $k_{\min}$, which represents the minimum allowed value of k on the network ($k_{\min} = 2$ here), and $k_{\max} \equiv k_{\min} N^{1/(\lambda-1)}$, which is the typical maximum degree of a network with N nodes [72, 73]. The scale-free feature allows a network to have some nodes with a large number of links ("hubs"), unlike the case for the classic Erdős-Rényi model of random networks [33, 74].

Here we show that for scale-free networks with $\lambda \geq 2$, transport properties characterized by conductance display a power-law tail distribution that is related to the degree distribution $P(k)$. We find that this power-law tail represents pairs of nodes of high degree which have high conductance. Thus, transport in scale-free networks is better than in Erdős-Rényi random networks. Also, we present a simple physical picture of transport in complex networks and test it with our data.

The classic random networks of Erdős and Rényi [33, 74] have a Poisson degree distribution, in contrast to the power-law distribution of the scale-free case. Due to the exponential decay of the degree distribution, the Erdős-Rényi networks lack hubs and their properties, including transport, are controlled solely by the average degree $\overline{k} \equiv \sum_{i=k_{\min}}^{k_{\max}} iP(i)$ [74, 75].

Most of the work done so far regarding complex networks has concentrated on static topological properties or on models for their growth [32, 72, 76, 77]. Transport features have not been extensively studied with the exception of random walks

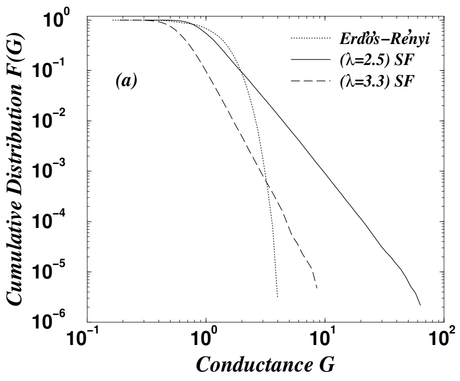

Figure 4.1: (a) Comparison for networks with $N = 8000$ nodes between the cumulative distribution functions for the Erdős-Rényi and the scale-free cases (with $\lambda = 2.5$ and 3.3). Each curve represents the cumulative distribution $F(G)$ vs. G. The simulations have at least 10^6 realizations.

on complex networks [78, 79, 80], despite the fact that transport properties contain information about network function [81]. Here, we study the electrical conductance G between two nodes A and B of Erdős-Rényi and scale-free networks when a potential difference is imposed between them. We assume that all the links have equal resistances of unit value [82].

To construct an Erdős-Rényi network, we begin with a fully connected network, and randomly remove $1 - \overline{k}/(N-1)$ out of the $N(N-1)/2$ links between the N nodes. To generate a scale-free network with N nodes, we use the Molloy-Reed algorithm [83], which allows for the construction of random networks with arbitrary degree distribution. We generate k_i copies of each node i, where the probability of having k_i satisfies Eq. (4.1). These copies of the nodes are then randomly paired in order to construct the network, making sure that two previously-linked nodes are not connected again, and also excluding links of a node to itself [84].

The conductance G of the network between two nodes A and B is calculated using the Kirchhoff method [85], where entering and exiting potentials are fixed to $V_A = 1$

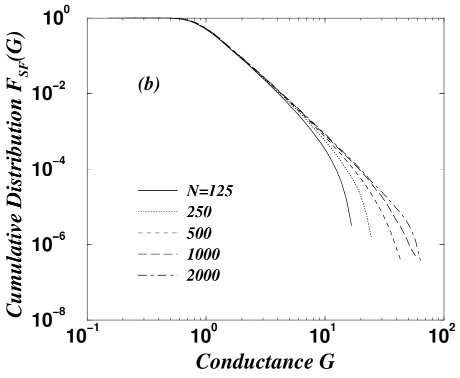

Figure 4.2: Effect of system size on $F_{\mathrm{SF}}(G)$ vs. G for the case $\lambda = 2.5$. The cutoff value of the maximum conductance $G_{\max}$ progressively increases as N increases.

and $V_B = 0$. We solve a set of linear equations to determine the potentials V_i of all nodes of the network. Finally, the total current $I \equiv G$ entering at node A and exiting at node B is computed by adding the outgoing currents from A to its nearest neighbors through $\sum_j (V_A - V_j)$, where j runs over the neighbors of A.

First, we analyze the pdf $\Phi(G)dG$ that two nodes on the network have conductance between G and $G+dG$. To this end, we introduce the cumulative distribution $F(G) \equiv \int_G^\infty \Phi(G')dG'$, shown in Fig. 4.1 for the Erdős-Rényi and scale-free ($\lambda = 2.5$ and $\lambda = 3.3$, with $k_{\min} = 2$) cases. We use the notation $\Phi_{\mathrm{SF}}(G)$ and $F_{\mathrm{SF}}(G)$ for scale-free, and $\Phi_{\mathrm{ER}}(G)$ and $F_{\mathrm{ER}}(G)$ for Erdős-Rényi. The function $F_{\mathrm{SF}}(G)$ for both $\lambda = 2.5$ and 3.3 exhibits a tail region well fit by the power law

$$F_{\mathrm{SF}}(G) \sim G^{-(g_G - 1)}, \tag{4.2}$$

and the exponent $(g_G - 1)$ increases with λ. In contrast, $F_{\mathrm{ER}}(G)$ decreases exponentially with G.

Increasing N does not significantly change $F_{\mathrm{SF}}(G)$ (Fig. 4.2) except for an increase in the upper cutoff $G_{\max}$, where $G_{\max}$ is the typical maximum conductance, corresponding to the value of G at which $\Phi_{\mathrm{SF}}(G)$ crosses over from a power law to a faster decay. We observe no change of the exponent g_G with N. The increase of $G_{\max}$ with

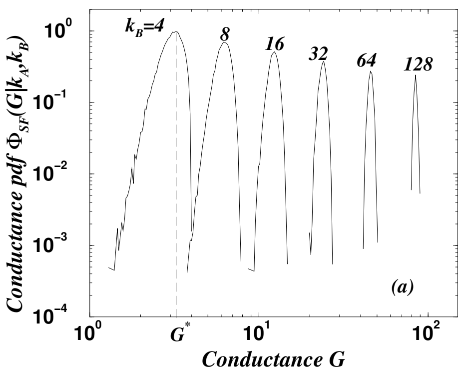

Figure 4.3: Probability density function $\Phi_{\mathrm{SF}}(G|k_A, k_B)$ vs. G for $N = 8000$, $\lambda = 2.5$ and $k_A = 750$ (k_A is close to the typical maximum degree $k_{\max} = 800$ for $N = 8000$).

N implies that the average conductance $\overline{G}$ over all pairs also increases slightly [86].

We next study the origin of the large values of G in scale-free networks and obtain an analytical relation between λ and g_G. Larger values of G require the presence of many parallel paths, which we hypothesize arise from the high degree nodes. Thus, we expect that if either of the degrees k_A or k_B of the entering and exiting nodes is small, the conductance G between A and B is small since there are at most k different parallel branches coming out of a node with degree k. Thus, a small value of k implies a small number of possible parallel branches, and therefore a small value of G. To observe large G values, it is therefore necessary that both k_A and k_B be large.

We test this hypothesis by large scale computer simulations of the conditional pdf $\Phi_{\mathrm{SF}}(G|k_A, k_B)$ for specific values of the entering and exiting node degrees k_A and k_B. Consider first the case $k_B \ll k_A$, and the effect of increasing k_B, with k_A fixed. We find that $\Phi_{\mathrm{SF}}(G|k_A, k_B)$ is narrowly peaked (Fig. 4.3) so that it is well characterized by G^*, the value of G when Φ_{SF} is a maximum. We find similar results for Erdős-Rényi networks. Further, for increasing values of k_B, we find [Fig. 4.4] G^* increases as $G^* \sim k_B^{\alpha}$, with $\alpha = 0.96 \pm 0.05$ consistent with the possibility that as $N \to \infty$, $\alpha = 1$ which we assume henceforth.

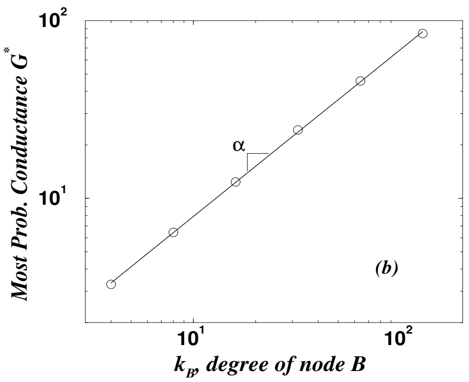

Figure 4.4: Most probable values of G^*, estimated from the maxima of the distributions in Fig. 4.3, as a function of the degree k_B. The data support a power law behavior $G^* \sim k_B^\alpha$ with exponent $\alpha = 0.96 \pm 0.05$.

For the case of $k_B \gtrsim k_A$, G^* increases less fast than k_B, as can be seen in Fig. 4.5 where we plot G^*/k_B against the scaled degree $x \equiv k_A/k_B$. The collapse of G^*/k_B for different values of k_A and k_B indicates that G^* scales as

$$G^* \sim k_B f\left(\frac{k_A}{k_B}\right). \tag{4.3}$$

The behavior of the scaling function $f(x)$ can be interpreted using the following simplified "transport backbone" picture [Fig. 4.5 inset], for which the effective conductance G between nodes A and B satisfies

$$\frac{1}{G} = \frac{1}{G_A} + \frac{1}{G_{tb}} + \frac{1}{G_B}, \tag{4.4}$$

where $1/G_{tb}$ is the resistance of the "transport backbone" while $1/G_A$ (and $1/G_B$) are the resistances of the set of bonds near node A (and node B) not belonging to the "transport backbone". It is plausible that G_A is linear in k_A, so we can write $G_A = ck_A$. Since node B is equivalent to node A, we expect $G_B = ck_B$. Hence

$$G = \frac{1}{1/ck_A + 1/ck_B + 1/G_{tb}} = k_B \frac{ck_A/k_B}{1 + k_A/k_B + ck_A/G_{tb}}, \tag{4.5}$$

so the scaling function defined in Eq. (4.3) is

$$f(x) = \frac{cx}{1 + x + ck_A/G_{tb}} \approx \frac{cx}{1+x}. \tag{4.6}$$

The second equality follows if there are many parallel paths on the "transport backbone" so that $1/G_{tb} \ll 1/ck_A$ [87]. The prediction (4.6) is plotted in Fig. 4.5 for both scale-free and Erdős-Rényi networks and the agreement with the simulations supports the approximate validity of the transport backbone picture of conductance in complex networks.

The agreement of (4.6) with simulations has a striking implication: the conductance of a complex network (scale-free and Erdős-Rényi) depends on only one parameter c. Further, since the distribution of Fig. 4.3 is sharply peaked, a single measurement of G for any values of the degrees k_A and k_B of the entrance and exit nodes suffices to determine G^*, which then determines c and hence through Eq. (4.6) the conductance for all values of k_A and k_B.

Within this "transport backbone" picture, we can analytically calculate $F_{\mathrm{SF}}(G)$. Using Eq. (4.3), and the fact that $\Phi_{\mathrm{SF}}(G|k_A, k_B)$ is narrow, yields [88]

$$\Phi_{\mathrm{SF}}(G) \sim \int P(k_B)dk_B \int P(k_A)dk_A \delta\left[k_B f\left(\frac{k_A}{k_B}\right) - G\right], \tag{4.7}$$

where $\delta(x)$ is the Dirac delta function. Performing the integration of Eq. (4.7) using (4.6), we obtain for $G < G_{\max}$

$$\Phi_{\mathrm{SF}}(G) \sim G^{-g_G} \qquad [g_G = 2\lambda - 1]. \tag{4.8}$$

Hence, for $F_{\mathrm{SF}}(G)$, we have $F_{\mathrm{SF}}(G) \sim G^{-(2\lambda-2)}$. To test this prediction, we perform simulations for scale-free networks and calculate the values of $g_G - 1$ from the slope of a log-log plot of the cumulative distribution $F_{\mathrm{SF}}(G)$. From Fig. 4.7 we find that

$$g_G - 1 = (1.97 \pm 0.04)\lambda - (2.01 \pm 0.13). \tag{4.9}$$

Thus, the measured slopes are consistent with the theoretical value predicted by Eq. (4.8) [89].

Next, we consider some further implications of our work. Our results show that larger values of G are found in scale-free networks with a much larger probability than in Erdős-Rényi networks, which raises the question if scale-free networks have better transport than Erdős-Rényi networks. To answer this question, we consider the average conductance between all the pairs of nodes in the network, which quantifies how efficient is the transport. However, since scale-free networks are heterogeneous, we must find a way to assign proper weights to the nodes. Recent work [90, 91] suggests that the conductance of links between nodes i and j in certain real-world networks are characterized by $(k_i k_j)^\beta$, with $\beta = 1/2$. Using this weight, and comparing scale-free and Erdős-Rényi networks with equal values of $\overline{k}$ [92], we find that the average conductance of scale-free networks is large than that of Erdős-Rényi networks (Table 4.1). Even larger average conductance for scale-free networks compared to Erdős-Rényi networks (Table 4.1) is obtained if one assumes [78] $\beta = 1$, i.e., that transport occurs with frequency proportional to the degree of the node. The case of $\beta = 0$ represents a "democratic" average, where all the pairs of nodes A and B are given the same weight. This case, which is not justified for heterogeneous networks, yields average conductance values for scale-free networks close to those of Erdős-Rényi networks (Table 4.1). In many real-world systems, degree dependent link conductances and frequent use of high degree nodes both occur, making scale-free network transport even more efficient than Erdős-Rényi network transport.

In summary, we find a power-law tail for the distribution of conductance for scale-free networks and relate the tail exponent g_G to the exponent λ of the distribution $P(k)$. Our work is consistent with a simple physical picture of how transport takes place in complex networks.

scale-free		$\beta = 1$	$\beta = 1/2$	$\beta = 0$
λ	$\overline{k}$	$\overline{G}_{SF}$ ($\overline{G}_{ER}$)	$\overline{G}_{SF}$ ($\overline{G}_{ER}$)	$\overline{G}_{SF}$ ($\overline{G}_{ER}$)
2.5	5.3	5.5 (2.1)	2.4 (2.0)	1.3 (1.9)
2.7	4.3	2.7 (1.5)	1.8 (1.5)	1.1 (1.4)
2.9	3.7	1.7 (1.2)	1.4 (1.2)	0.9 (1.1)
3.1	3.4	1.3 (1.0)	1.1 (0.9)	0.8 (0.9)
3.3	3.1	1.0 (0.9)	1.0 (0.8)	0.7 (0.7)
3.5	2.9	0.8 (0.7)	0.8 (0.7)	0.6 (0.7)

Table 4.1: Values of average conductance of scale-free and Erdős-ényi networks for weights defined as $(k_i k_j)^\beta$. In parenthesis we have indicated the values of the corresponding Erdős-Rényi networks.

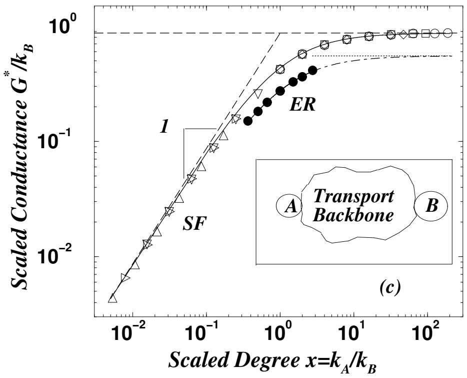

Figure 4.5: Scaled most probable conductance G^*/k_B vs. scaled degree $x \equiv k_A/k_B$ for system size $N = 8000$ and $\lambda = 2.5$, for several values of k_A and k_B: $\square$ ($k_A = 8$, $8 \leq k_B \leq 750$), $\diamondsuit$ ($k_A = 16$, $16 \leq k_B \leq 750$), $\triangle$ ($k_A = 750$, $4 \leq k_B \leq 128$), $\bigcirc$ ($k_B = 4$, $4 \leq k_A \leq 750$), $\bigtriangledown$ ($k_B = 256$, $256 \leq k_A \leq 750$), and $\triangleright$ ($k_B = 500$, $4 \leq k_A \leq 128$). The solid line crossing the symbols is the predicted function $G^*/k_B = cx/(1+x)$ obtained from Eq. (4.6). We also show G^*/k_B vs. scaled degree $x \equiv k_A/k_B$ for Erdős-Rényi networks with $\overline{k} = 2.92$ and $4 \leq k_A \leq 11$ and $k_B = 4$ (symbol $\bullet$), the solid line crossing the symbols representing the theoretical result according to Eq. (4.6), and an extension of this line to represent the limiting value of G^*/k_B (dotted-dashed line). Note that the probability to obtain $k_A > 11$ is extremely small in Erdős-Rényi networks, and thus we are unable to obtain significant statistics. These plots show the rapid approach of the scaling function $f(x)$ of Eq. (4.6) from a linear behavior to the constant c (here $c = 0.87 \pm 0.02$ for scale-free networks, horizontal dashed line, and $c = 0.55 \pm 0.01$ for Erdős-Rényi, dotted line). The inset shows a schematic of the "transport backbone" picture, where the circles labeled A and B denote the nodes A and B and their associated links which do not belong to the "transport backbone".

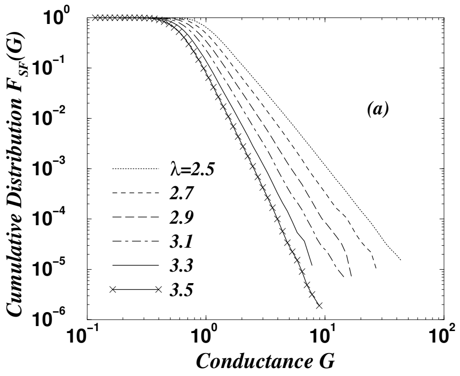

Figure 4.6: Simulation results for the cumulative distribution $F_{\rm SF}(G)$ for λ between 2.5 and 3.5, consistent with the power law $F_{\rm SF} \sim G^{-(g_G-1)}$ (cf. Eq. (4.8)), showing the progressive change of the slope $g_G - 1$.

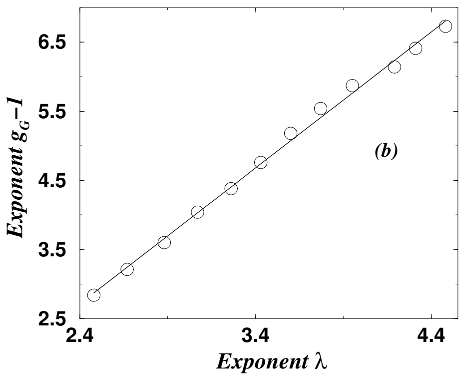

Figure 4.7: (b) The exponent $g_G - 1$ from simulations (circles) with $2.5 < \lambda < 4.5$; shown also is a least square fit $g_G - 1 = (1.97 \pm 0.04)\lambda - (2.01 \pm 0.13)$, consistent with the predicted expression $g_G - 1 = 2\lambda - 2$ [cf. Eq. (4.8)].

Part IV

Appendix

Solving the Kirchhoff Equations

Since both problems considered require the solution of the Kirchhoff Equations, we present a description of the method.

First, consider a connected graph with N sites. These sites are interconnected based on the structure of the lattice under consideration. For a two-dimensional square lattice, for instance, each site is connected to four neighbors which surround the site. For Erdős-Rényi random graphs, a site has a random number of neighbors that varies from site to site and satisfies Eq. (1.4).

In either case, if we are interested in solving the circuit equations, we must begin by choosing one or more sites as the source, which we label A, and one or more sites as the sink, which we label B. The simplest case corresponds to A being only one site, and B being another site. We impose values of the potential V_A and $V_B = 0$. The value of V_A is one for the case of constant pressure conditions (for percolation this is one of two situations, and this is the only situation studied for complex networks). For constant current conditions, $V_A = R$, where R is the total resistance of the particular realization being studied.

Having considered the boundary conditions, we now explain how to solve for the values of potential V_i at each site i, and the values of current I_{ij} along link ij. First, we point out that it is necessary to use only one of the two Kirchhoff rules in order to solve the problem completely. Here, we choose to apply the current rule, which states that at all sites of the network current is conserved. Thus, the sum of all incoming current to a site is equal to the sum of all outgoing current from the site. Now, since we assume ohmic circuits throughout this work, the current from site i to site j along link ij, with resistance r_{ij}, is given by

$$I_{ij} = \frac{V_i - V_j}{r_{ij}}. \tag{4.10}$$

In our study, the resistance from site i to site j is the same as from site j to site i, and thus

$$r_{ij} = r_{ji}. \tag{4.11}$$

Kirchhoff's current conservation law then implies

$$\sum_{j=1}^{N} I_{ij} = \sum_{j=1}^{N} \frac{V_i - V_j}{r_{ij}} = I(\delta_{iA} - \delta_{iB}), \tag{4.12}$$

where I represents the total current entering the circuit through A and leaving it through B and δ_{nm} represents the Kronecker delta

$$\delta_{nm} = \begin{cases} 0 & n \neq m \\ 1 & n = m. \end{cases} \tag{4.13}$$

Equation (4.12) expresses the fact that for all sites except the source and sink, the total in- plus out-current is zero.

Considering that V_A and V_B are known, there $N-2$ Eqs. (4.12) (A and B are the only sites not counted) and $N-2$ unknown potentials V_i, where $i = 1, \ldots, N$ except A and B. Therefore, we need to solve the system of equations

$$\mathbf{TV} = \mathbf{S}, \tag{4.14}$$

where matrices $\mathbf{T}, \mathbf{V}$ and $\mathbf{S}$ are given by

$$\mathbf{T} = \begin{vmatrix} \sum_{j=1,\, j\neq 1}^{N} \frac{1}{r_{1j}} & -\frac{1}{r_{12}} & \cdots & -\frac{1}{r_{1N}} \\ -\frac{1}{r_{21}} & \sum_{j=1,\, j\neq 2}^{N} \frac{1}{r_{2j}} & \cdots & -\frac{1}{r_{2N}} \\ \vdots & \vdots & \vdots & \vdots \\ -\frac{1}{r_{N1}} & -\frac{1}{r_{N2}} & \cdots & \sum_{j=1,\, j\neq N}^{N} \frac{1}{r_{Nj}} \end{vmatrix}, \tag{4.15}$$

$$\mathbf{V} = \begin{vmatrix} V_1 \\ V_2 \\ \vdots \\ V_N \end{vmatrix}, \tag{4.16}$$

and

$$\mathbf{S} = \begin{vmatrix} \frac{V_A}{r_{1A}} + \frac{V_B}{r_{1B}} \\ \vdots \\ \frac{V_A}{r_{NA}} + \frac{V_B}{r_{NB}} \end{vmatrix}. \tag{4.17}$$

None of the matrices have the A or B row. In other words, these rows are not used.

Aside from the symmetry expressed in Eq. (4.11), there is one further simplification for both of our transport models. The values of resistance are all taken to be identical to one. Thus matrix $\mathbf{T}$ becomes the so called Laplacian matrix $\mathbf{L}$, which is the matrix that represents the Laplacian operator in discrete space. It is defined by

$$(\mathbf{L})_{ij} = \begin{cases} k_i & i = j \\ -c_{ij} & i \neq j. \end{cases} \tag{4.18}$$

where k_i is the degree of node i as before, and $c_{ij} = 1$ if sites i and j are connected, and zero otherwise. The matrix of the c_{ij} is called the connectivity or adjacency matrix.

The solution to this system of equations if perfomed through the use of linear algebra software packages. Typically, matrix $\mathbf{T}$ is sparse, thus a high efficiency can be achieved with a computational complexity that is slower than N^2. Thus, the matrix inversion is relatively fast.

Part V

References

LIST OF ABBREVIATIONS

1. Advances in Physics (Adv. Phys.).
2. AIChE Journal (AIChE J.).
3. Annals of Physical Chemistry (Ann. Phys. Chem.).
4. Chemical Engineering Communications (Chem. Eng. Commun.).
5. Chemical Engineering Science (Chem. Eng. Sci.).
6. The European Physical Journal B (Eur. Phys. J. B).
7. Journal de Physique (J. Phys.)
8. Journal of Fluid Mechanics (J. Fluid Mech.).
9. Journal of Geophysical Research. Solid Earth. Series B (J. Geophys. Res. B).
10. Journal of the London Mathematical Society (J. Lond. Math. Soc.).
11. Journal of Physics A (J. Phys. A).
12. Journal of Statistical Physics (J. Stat. Phys.).
13. Proceedings of the Cambridge Phylosophical Society (Proc. Camb. Phyl. Soc.).
14. Physica (Phys.).
15. Physical Review A (Phys. Rev. A).
16. Physical Review B (Phys. Rev. B).
17. Physical Review E (Phys. Rev. E).
18. Physical Review Letters (Phys. Rev. Lett.).
19. Physics Letters A (Phys. Lett. A).
20. Publicationes Mathematicae (Publ. Math.).
21. Random Structures and Algorithms (Random Struct. Algorithms).
22. Reviews of Modern Physics (rev. Mod. Phys.).

Bibliography

[1] P. R. King in *North Sea Oil and Gas Reservoirs Conference III*, edited by A. T. Buller (Graham and Trotman, London, 1990).

[2] D. Stauffer and A. Aharony, *Introduction to Percolation Theory*, 2nd. edition (Taylor and Francis, London, 1994).

[3] M. Sahimi, *Flow and Transport in Porous Media and Fractured Rock* (VCH, Boston, MA 1995).

[4] M. Sahimi, *Applications of Percolation Theory* (Taylor & Francis, London, 1994).

[5] *Fractals and Disordered Systems*, 2nd. ed., edited by A. Bunde and S. Havlin (Springer, Berlin 1996).

[6] D. Ben-Avraham and S. Havlin, *Diffusion and Reactions in Fractals and Disordered Systems* (Cambridge University Press, Cambridge, 2000).

[7] J. M. Ziman, *Models of Disorder* (Cambridge University Press, Cambridge, 1979).

[8] *The Fractal Approach to Heterogeneous Chemistry: Surfaces, Colloids, Polymers*, edited by D. Avnir (John Wiley & Sons, Chichester, U.K. 1989).

[9] S. Havlin and D. Ben-Avraham, Adv. Phys. **36**, 695 (1987).

[10] P. G. Saffman, J. Fluid Mech. **6**, 321 (1959).

[11] N. V. Dokholyan, Y. Lee, S. V. Buldyrev, S. Havlin, P. R. King and H. E. Stanley. J. Stat. Phys. **93**, 603 (1998).

[12] Y. Lee, J. S. Andrade, S. V. Buldyrev, N. V. Dokholyan, S. Havlin, P. R. King, G. Paul, H. E. Stanley, Phys. Rev. E **60**, 3425 (1999).

[13] J. S. Andrade, S. V. Buldyrev, N. V. Dokholyan, S. Havlin, P. R. King, Y. Lee, G. Paul, H.E. Stanley, Phys. Rev. E **62**, 8270 (2000).

[14] J.-C. Bacri *et al.*, in *Hydrodynamics of Dispersed Media*, edited by J. P. Hulin, A. M. Cazabat, E. Guyon, and F. Carmona (Elsevier/North-Holland, Amsterdam, 1990), p. 249.

[15] J. Koplik, S. Redner, D. Wilkinson, Phys. Rev. A **37**, 2619 (1988).

[16] V. Ambegaokar, B. I. Halperin, and J. S. Langer, Phys. Rev. B **4**, 2612 (1971).

[17] M. Sahimi, Rev. Mod. Phys. **65**, 1393 (1993).

[18] E. T. Gawlinski and H. E. Stanley, J. Phys. A **14**, L291 (1981).

[19] A. Geiger and H. E. Stanley, Phys. Rev. Lett. **49**, 1895 (1982).

[20] A. J. Katz and A. H. Thompson, Phys. Rev. B **34**, 8179 (1986); J. Geophys. Res. B **92**, 599 (1987).

[21] Hernan A. Makse, Glenn W. Davies, Shlomo Havlin, Plamen Ch. Ivanov, Peter R. King, and H. E. Stanley, Phys. Rev. E **54**, 3129 (1996).

[22] T. A. Hewett (unpublished); T. A. Hewett and R. A. Behrens, SPE Formation Evaluation **5**, 217 (1990).

[23] A. D. Araújo, A. A. Moreira, H. A. Makse, H. E. Stanley, and J. S. Andrade, Phys. Rev. E **66**, 046304 (2002).

[24] M. Sahimi, J. Phys. (France) I **4**, 1263 (1994); M. Sahimi and M. A. Knackstedt, *ibid.* **4**, 1269 (1994); M. Sahimi, AIChE J. **41**, 229 (1995).

[25] S. Prakash, S. Havlin, M. Schwartz, and H. E. Stanley, Phys. Rev. A **46**, R1724 (1992).

[26] S. R. Broadbent and J. M. Hammersley, Proc. Camb. Phyl. Soc. **53**, 629 (1957).

[27] A. Bunde and S. Havlin, eds. *Fractals and Disordered Systems*, 2nd ed. (Springer, Berlin, 1996).

[28] A. Bunde, S. Havlin, R. Nossal, H. E. Stanley, and G. H. Weiss, J. Chem. Phys., **83**, 5909 (1985).

[29] B. Mandelbrot, *The Fractal Geometry of Nature* (W. H. Freeman, 1982).

[30] E. López, S. V. Buldyrev, N. V. Dokholyan, L. Goldmakher, S. Havlin, P. R. King, and H. E. Stanley, Phys. Rev. E **67**, 056314 (2003).

[31] M. Cieplak et al., A. Maritan, and J. R. Banavar, Phys. Rev. Lett. **72**, 2320 (1994).

[32] R. Albert and A.-L. Barabási. Rev. Mod. Phys. **74**, 47 (2002); R. Pastor-Satorras and A. Vespignani, *Structure and Evolution of the Internet: A Statistical Physics Approach* (Cambridge University Press, Cambridge, 2004); S. N. Dorogovsetv and J. F. F. Mendes, *Evolution of Networks: From Biological Nets to the Internet and WWW* (Oxford University Press, Oxford, 2003).

[33] P. Erdős and A. Rényi, Publ. Math. (Debrecen), **6**, 290 (1959).

[34] S. Sreenivasan, T. Kalisky, L. A. Braunstein, S. V. Buldyrev, S. Havlin, and H. E. Stanley, Phys. Rev. E 70, 046133 (2004).

[35] Z. Alexandrowicz, Phys. Lett. **80A**, 284 (1980).

[36] R. Pike and H. E. Stanley, J. Phys. A **14**, L169 (1981).

[37] H. J. Herrmann and H. E. Stanley, J. Phys. A **21**, L829 (1988).

[38] P. Grassberger, J. Phys. A **25**, 5475 (1992).

[39] P. Ray, J. Phys. A **18**, L657 (1985).

[40] M. Barma and P. Ray, Phys. Rev. B **34**, 3403 (1986).

[41] A. U. Neumann and S. Havlin, J. Stat. Phys. **52**, 203 (1988).

[42] R. M. Ziff, J. Phys. A **32**, L457 (1999).

[43] J. R. de Dreuzy, P. Davy, B. Berkowitz, Phys. Rev. E **64**, 056305 (2001).

[44] See e.g., J. G. Zabolitzky, Phys. Rev. B **30**, 4077 (1984); H. J. Herrmann, B. Derrida, and J. Vannimenus, *ibid.*, **30**, 4080 (1984); D. C. Hong, S. Havlin, H. J. Herrmann, and H. E. Stanley, *ibid.*, **30**, 4083 (1984); C. J. Lobb and D. J. Frank, *ibid.*, **30**, 4090 (1984); L. de Arcangelis, S. Redner, and A. Coniglio, *ibid.*, **31**, 4725 (1985).

[45] M. Barthélémy, S. V. Buldyrev, S. Havlin, H. E. Stanley, Phys. Rev. E **61**, R3283 (2000).

[46] L. Paterson, Phys. Rev. Lett. **52**, 1621 (1984).

[47] J. D. Sherwood and J. Nittmann, J. Phys. (Paris) **47**, 15 (1986)

[48] P. R. King, J. Phys. A **20**, L529 (1987).

[49] M. Murat and A. Aharony, Phys. Rev. Lett. **57**, 1875 (1986).

[50] J. S. Andrade, A. D. Araujo, S. V. Buldyrev, S. Havlin, and H. E. Stanley, Phys. Rev. E **63**, 051403 (2001).

[51] S. Redner, *A Guide to First-Passage Processes* (Cambridge University Press, Cambridge, 2001).

[52] J. Koplik, S. Redner and E. J. Hinch, Phys. Rev. E **50**, 4650 (1994).

[53] M. Sahimi, H. T. Davis, and L. E. Scriven, Chem. Eng. Commun. **23**, 329 (1983); M. Sahimi, A. L. Heiba, B. D. Hughes, L. E. Scriven, and H. T. Davis, Chem. Eng. Sci. **41**, 2103 (1986); **41**, 2123 (1986); M. Sahimi and A. O. Imdakm, J. Phys. A **21**, 3833 (1988).

[54] P. Grassberger, Physica A **262**, 251 (1999).

[55] G. Paul, S. V. Buldyrev, N. V. Dokholyan, S. Havlin, P. R. King, Y. Lee and H. E. Stanley, Phys. Rev. E **61**, 3435 (2000).

[56] G. G. Batrouni, A. Hansen, and S. Roux, Phys. Rev. A **38**, 3820 (1988).

[57] M. Barthélémy, S. V. Buldyrev, S. Havlin, and H. E. Stanley, Phys. Rev. E **60**, R1123 (1999).

[58] D. ben-Avraham and S. Havlin, *Diffusion and Reactions in Fractals and Disordered Systems* (Cambridge University Press, Cambridge, 2000).

[59] S. Havlin and D. ben-Avraham, Adv. Phys. **36**, 695 (1987).

[60] A. Bunde and S. Havlin, eds. *Fractals and Disordered Systems*, 2nd ed. (Springer, Berlin, 1996).

[61] M. Porto, S. Havlin, H. E. Roman, and A. Bunde, Phys. Rev. E **58**, R5205 (1998).

[62] Z. Wu, E. López, L. Braunstein, S. V. Buldyrev, S. Havlin, and H. E. Stanley, Phys. Rev. E **71**, 045101 (2005).

[63] L. A. Braunstein, S. V. Buldyrev, S. Havlin, and H. E. Stanley, Phys. Rev. E **65**, 056128 (2002); S. Sreenivasan et al. (preprint).

[64] S. V. Buldyrev, L. A. Braunstein, R. Cohen, S. Havlin, and H. E. Stanley, Physica A **330** 246 (2003).

[65] Since most of the computational demands come from checking connectivity between A and B, we use the method in Ref. [64], which consists of finding the shortest path between A and B, and then, as long as none of the sites of this shortest path are bombed, it is not necessary to check connectivity. Only when a site of the shortest path is bombed, connectivity is checked. If there is a new shortest path, the site is eliminated, but if there is no alternative path, then the site belongs to the optimal path and the shortest path is kept.

[66] S. V. Buldyrev, S. Havlin, E. López, and H. E. Stanley, Phys. Rev. E **70**, 035102(R) (2004).

[67] S. Havlin and D. ben-Avraham, Adv. Phys. **36**, 695 (1987).

[68] N. V. Dokholyan., Y. K. Lee, S. V. Buldyrev, S. Havlin, P. R. King, and H. E. Stanley, J. Stat. Phys. **93**, 603 (1998).

[69] P. L. Leath, Phys. Rev. B **14**, 5046 (1976).

[70] M. Cieplak et al., A. Maritan, and J. R. Banavar, Phys. Rev. Lett. **76**, 3754 (1996).

[71] A.-L. Barabási and R. Albert, Science **286**, 509 (1999).

[72] R. Cohen et al., Phys. Rev. Lett. **85**, 4626 (2000).

[73] In principle, a node can have a degree up to $N-1$, connecting to all other nodes of the network. The results presented here corresponds to networks with

the upper cutoff $k_{\max} = k_{\min} N^{1/(\lambda-1)}$ imposed. We also studied networks for which this cutoff is not imposed, and found no significant differences in the pdf $\Phi_{\rm SF}(G)$.

[74] B. Bollobás, *Random Graphs* (Academic Press, Orlando, 1985).

[75] G. R. Grimmett and H. Kesten, J. Lond. Math. Soc. **30**, 171 (1984); G. R. Grimmett and H. Kesten, math/0107068.

[76] P. L. Krapivsky et al., Phys. Rev. Lett. **85**, 4629 (2000).

[77] Z. Toroczkai and K. Bassler, Nature **428**, 716 (2004).

[78] J. D. Noh and H. Rieger, Phys. Rev. Lett. **92**, 118701 (2004).

[79] V. Sood, S. Redner, and D. ben-Avraham, cond-mat/0410309.

[80] L. K. Gallos, Phys. Rev. E **70**, 046116 (2004).

[81] The dynamical properties that we study here are related to transport on networks and differ from those which treat the network topology itself as evolving in time [71, 76].

[82] The study of community structure has led some authors (M. E. J. Newman and M. Girvan, Phys. Rev. E **69**, 026113 (2004), and F. Wu and B. A. Huberman, Eur. Phys. J. B **38**, 331 (2004)) to propose methods in which networks are considered as electrical networks in order to identify communities. In these studies, however, transport properties have not been addressed.

[83] M. Molloy and B. Reed, Random Struct. Algorithms **6**, 161 (1995).

[84] We performed simulations with the node copies randomly matched, and also matched in order of degree from highest to lowest and obtained similar results.

[85] G. Kirchhoff, Ann. Phys. Chem. **72**, 497 (1847); N. Balabanian, *Electric Circuits* (McGraw-Hill, New York, 1994).

[86] Since $g_G > 2$ for $\lambda > 2$, it follows that although $\bar{G}$ increases with N, it finally converges to a constant. Only for $g_G < 2$, the cutoff $G_{\max}$ in the tail of $\Phi_{\rm SF}(G)$ controls $\bar{G}$, making $\bar{G}$ an increasing unbounded function of N.

[87] Flux starts at node A, being controlled by the conductance of the bonds in the vicinity of node A. This flux passes into the "transport backbone", which is comprised of many parallel paths and hence has a high conductance. Finally, flux ends at node B, being controlled by the conductance of the bonds in the vicinity of node B. This is similar to the traffic around a major freeway. Most of the limitations to transport occur in getting to the freeway ("node A") and then after leaving it ("node B"), but flow occurs easily on the freeway ("transport backbone").

[88] N. G. Van Kampen, *Stochastic Processes in Physics and Chemistry* (North-Holland, Amsterdam, 1992).

[89] The λ values explored here are limited by computer time considerations. In principle, we are unaware of any theoretical reason that would limit the validity of our results to any particular range of values of λ (above 2).

[90] E. Almaas, S. Redner, and P. Krapivski, Phys. Rev. E (in press) (2005).

[91] K.-I. Goh, B. Kahng, and D. Kim, cond-mat/0410078.

[92] The cost of a network is defined as its number of links. Two networks with equal N and equal $\overline{k}$ have the same cost. We compare scale-free and Erdős-Rényi networks of equal cost.

Part VI

Curriculum Vitae

Chapter 5

Curriculum Vitae

Contact Information

Center for Polymer Studies

Physics Department

590 Commonwealth Ave.

Boston, MA 02215

1 617 353 4737	Citizenship: Venezuelan
email: edlopez@bu.edu	**Languages:** English, Spanish

Research Interests

- Flow in Complex geometries: Tracer flows in percolation and exponential disorder. Physical Flows in random and scale-free networks with an interest in their applicability to real world problems.

- Effect of disorder on optimization problems. Fractal properties of optimal path lengths in broadly disordered systems.

- Surface growth dynamics. Behavior of a crystalline growing interface in the presence of long range interactions. Highly disordered soliton gases.

Academic Background

- **Undergraduate Studies:** December, 1995. Licenciado en Física, Universidad del Zulia, Maracaibo, Venezuela. Graduated Summa Cum Laude (first ever awarded to a Physics graduate at this institution).

- **Graduate Studies:** January 2000. Master of Arts in Physics, Boston University, Boston, Massachusetts, United States.

- **Current Studies:** Currently in PhD program, Boston University, Boston, Massachusetts, United States.

Relevant Skills

- Mathematical Tools for the study of Physical Systems.

- Computational Tools.

- Expertise in Numerical Methods.

Professional Work Experience

- Research Assistant. Center for Polymer Studies. Boston University. 9/98 to present

- Full time Faculty member. Boston University Academy. 9/2000 to 6/2001

- Interim Junior Professor. University of Zulia 1/96-8/97

- Visiting Collaborator. Computational Physics Laboratory. 11/95-5/97 Instituto Venezolano de Investigaciones Científicas (IVIC) [Venezuelan Institute for Scientific Research]

- Research Assistant. Computational Physics Laboratory. IVIC 9/94-11/95

Awards & Affiliations

- First ever Summa Cum Laude graduate of the Physics Department at University of Zulia.
- Teaching Fellow of the year award, voted by the Faculty of the Department of Physics of Boston University, for excellence in teaching for the academic year 2002-2003.
- Award from the Experimental College of Science, for achieving the highest GPA in the Physics program in Physics in 1994.
- MARAVEN Award to Academic Excellence, for attaining the highest GPA in 1993 in the Experimental College of Science. MARAVEN was a subsidiary of Venezuelan oil company PDVSA.
- Simón Rodríguez Award, for attaining the highest GPA in the Experimental College of Science. Two times: 1990 and 1993
- Honor Roll of the University of Zulia, for attaining one of the 10 highest GPA at Experimental College of Science. Obtained from 1990 to 1993
- Student member of the American Physical Society 2004.
- Member of the Venezuelan Physical Society. 1995-present

Publications

1. "Anomalous Transport in Complex Networks". Eduardo López, Sergey V. Buldyrev, Shlomo Havlin, and H. Eugene Stanley. Submitted to Phys. Rev. Lett. (cond-mat/0412030).

2. "Current Flow in Random Resistor Networks: The role of Percolation in Weak and Strong Disorder" Zhenhua Wu, Eduardo López, Lidia Braunstein, Sergey V. Buldyrev, Shlomo Havlin, and H. Eugene Stanley. Submitted to Phys. Rev. Lett. (cond-mat/0411062).

3. "Universality of the optimal path in the strong disorder limit". Sergey V. Buldyrev, Shlomo Havlin, Eduardo López, and H. Eugene Stanley, Phys. Rev. E **70** 035102 (2004).

4. "Post-breakthrough Behavior in Flow through Porous Media". Eduardo López, Sergey V. Buldyrev, Nikolay V. Dokholyan, Leo Goldmakher, Shlomo Havlin, Peter R. King, and H. Eugene Stanley, Phys. Rev. E **67**, 056314 (2003).

5. "Using percolation theory to predict oil field performance" Peter R. King, Sergey V. Buldyrev, Nikolay V. Dokholyan, Shlomo Havlin, Eduardo López E, Gerry Paul, and H. Eugene Stanley, Phys. A **314**(1-4), 103 (2002).

6. "Uncertainty in oil production predicted by percolation theory". Peter R. King, Sergey V. Buldyrev, Nikolay V. Dokholyan, Shlomo Havlin, Eduardo López E, Gerry Paul, and H. Eugene Stanley, Phys. A **306**(1-4), 376 (2002).

7. "Topological Defects with Long-Range Interactions". B. A. Mello, Jorge A. González, Luis E. Guerrero, and Eduardo López-Atencio, Phys. Lett. A **244**(4), 277 (1998).

8. "Long-Range Self-Affine Correlations in a Random Soliton Gas". Luis E. Guerrero, Eduardo López-Atencio, and Jorge A. González, Phys. Rev. E **55**(6), 7691 (1997).

Other Publications

1. "Physics of Flow in Random Media". Eduardo López. Ph. D. Thesis, Boston University, 2004.

2. "Performing the Cavendish Experiment". Eduardo López, Jason St. John, and B. Lee Roberts. Currently used lab manual for the Cavendish experiment at the Physics Department at Boston University.

3. "Transición al orden fractal en un sistema aleatorio tipo seno de Gordon". Eduardo López. Undergraduate thesis, Universidad del Zulia, Maracaibo, Venezuela, 1995.

Articles under preparation

1. "Distribution of the Optimal Path in Strong Disorder". Eduardo López, Lidia Braunstein, Sergey V. Buldyrev, Shlomo Havlin, and H. Eugene Stanley.

2. "Scale-free gradient networks". E. López, A. Clauset, C. Moore, and Z. Toroczkai.

3. "Structural Properties of gradient networks". E. López and Z. Toroczkai.

Media Interviews

- Interview by Esmeralda Stuk for The Daily Free Press, appearing in the 3/15/04 issue for the article "6 degrees of Kevin Bacon game real, says BU study". *http://www.dailyfreepress.com/news/2004/03/15/News/ 6.Degrees.Of.Kevin.Bacon.Game.Real.Says.Bu.Study-633462.shtml*

Presentations at Conferences

- "Flow in Percolation Clusters: Post-breakthrough behavior". Eduardo López, STATPHYS 21, Cancún, México, 2001.
- "Long Range Correlations in a Random sine-Gordon chain". Eduardo López Atencio; Luis E. Guerrero; Jorge A. González, Contributed work to the XLV Annual AsoVAC (Asociación Venezolana para el Avance de la Ciencia) Convention 1995. Caracas, Venezuela

References

1. Gene Stanley
   Professor
   Director, Center for Polymer Studies
   Boston University, 590 Commonwealth Ave., Boston, MA
   Phone: 1 617 353 2617
   email: hes@argento.bu.edu
2. Shlomo Havlin
   Professor
   Minerva Center and Department of Physics
   Bar-Ilan University, Ramat-Gan, Israel
   Phone: 972 3 531 8436
   email: havlin@ophir.ph.biu.ac.il
3. Sergey Buldyrev
   Professor
   Physics Department
   Yeshiva University, New York, NY

Phone: 1 212 960 5430

email: sergey@sled.mc.yu.edu

4. Peter R. King

   Professor

   Center for Petroleum Science, TH Huxley School

   Imperial College, London, United Kingdom

   Phone: 44 20 7594 7362

   email: peter.king@imperial.ac.uk

5. Nikolay V. Dokholyan

   Assistant Professor

   Department of Biochemistry and Biophysics,School of Medicine

   University of North Carolina at Chapel Hill, Chapel Hill, NC 27599

   Phone: 1 919 843 2513

   email: dokh@med.unc.edu

   Web: http://dokhlab.unc.edu/

6. Luis E. Guerrero

   Professor

   Departamento de Física

   Universidad Simón Bolivar, Caracas, Venezuela

   Phone: 58 202 5041389, 58 202 5041566

   email: lguerre@usb.ve

7. B. Lee Roberts

   Professor

   Physics Department

   Boston University, 590 Commonwealth Ave., Boston, MA

   Phone: 1 617 353 2187

email: roberts@buphy.bu.edu

8. Keneth Lane

   Professor

   Physics Department

   Boston University, 590 Commonwealth Ave., Boston, MA

   Phone: 1 617 353 4512

   email:lane@buphy.bu.edu